Vortex-Induced Vibrations of in-line cantilevered cylinders

Hussain, M. M.M.D.; Zwijsen, K.; van Zuijlen, A. H.

DOI
10.1016/j.compfluid.2025.106647

Publication date
2025

Document Version
Final published version

Published in
Computers and Fluids

Computers and Fluids 297 (2025) 106647

Contents lists available at ScienceDirect

Computers and Fluids

journal homepage: www.elsevier.com/locate/compfluid

Vortex-Induced Vibrations of in-line cantilevered cylinders

M.M.M.D. Hussain [a,*], K. Zwijsen [a], A.H. van Zuijlen [b]

[a] Nuclear Research and Consultancy Group (NRG), Westerduinweg 3, 1755LE Petten, The Netherlands
[b] Delft University of Technology (TU Delft), 2629HS Delft, The Netherlands

ARTICLE INFO

Keywords:
Vortex-Induced Vibrations
Fluid-Structure Interactions
Flow-Induced Vibrations
URANS
Turbulence Modelling
STAR-CCM+

ABSTRACT

The advent of global warming has brought an increased interest in non-conventional sources of energy, one of which is nuclear energy. Threatening the almost year-round functioning of nuclear power plants are Flow-Induced Vibrations (FIV). One mechanism of FIV, Vortex-Induced Vibration (VIV), holds importance in areas of cross-flow in nuclear power plants where lock-in occurs. To make safe-life designs, computational analysis in the domain of Fluid-Structure Interactions (FSI) has been increasing over the past two decades. This article aims to add to the body of knowledge by making predictions for an in-line two-cylinder configuration, set up as part of a benchmark proposed by the Nuclear Energy Agency (NEA) of the Organization for Economic Co-operation and Development (OECD), using the commercial code *Simcenter STAR-CCM+ (V2020.3.1)*.

The main objective of this study is to test the efficacy of the URANS framework in predicting VIV, which is connected with the objective of the OECD/NEA to propose recommendations for the *Best Practice Guidelines*. The benchmark was structured in two phases: the open phase where the experimental results were available to the benchmark participants a priori and the blind phase where the experimental results, with cylinders having different natural frequencies than that of the open phase, were released to the benchmark participants only after all computational results were submitted to the OECD/NEA. The open phase was used to test 3 turbulence models, namely 'K-ω SST: Quadratic', 'K-ω SST: Quadratic + GRT transition' and 'Standard K-ϵ Low Re: Cubic' in order to choose the most appropriate model for the blind phase. Key results from this study revealed the 'Standard K-ϵ Low Re: Cubic' model to be the most apt for the benchmark. Furthermore, gaps are also identified in the application of URANS to predict VIV resonance conditions, namely the overprediction of the vortex shedding frequency, adoption of inflow turbulence and the underprediction of high frequency range spectra.

1. Introduction

With an increasing worldwide human population comes an increasing energy demand. Different conventional and non-conventional sources of energy are available and their use has a direct link to global warming. The Intergovernmental Panel on Climate Change (IPCC) warns humanity about the effects of global warming of 1.5 °C above pre-industrial levels and related global greenhouse gas emission pathways [1]. Nuclear energy is a way to transition to a world with low carbon footprint as pointed out by many international studies especially when affordability of energy production is considered [1–7].

An advantage of nuclear power plants is its capability of producing electrical power almost year-round with the exception of a 3 week period of refuelling and maintenance. For economic benefit, it is desired that the plants run without any unplanned outages. Another reason for this is the possibility of the nuclear reactor to be unable to restart owing to the build-up of Xenon. After a power decrease or shutdown, it may take upto about 3 days before a typical reactor is able to override the effects of Xenon. Translating the time loss into money at a rate of 1 million euro per day, [8,9] the desire to avoid outages is made obvious.

A leading reason for the downtime is owed to damage as a result of Flow-Induced Vibrations (FIV), a term used to describe all the phenomena that are associated with the response of structures immersed in a flow. In literature for internal flows, this term is used for stationary (statistically steady) flow where interaction is mainly one-way from fluid to solid while the term Fluid-Structure Interactions (FSI) is used for two-way interactions in unsteady flows [10]. In this article, both terms are used interchangeably to imply any interaction between solid and fluid for nuclear applications. FIV has been pointed to be a cause of fatigue problems, stress corrosion, cracking, fretting wear and other possible failure modes in nuclear power plants [9,11–13]. Increasing energy demand leads to change of coolant, its flow rate or changes in component material and/or dimensions leading to more prominent FIV [14].

* Corresponding author.
E-mail addresses: hussain@nrg.eu (M.M.M.D. Hussain), zwijsen@nrg.eu (K. Zwijsen), a.h.vanzuijlen@tudelft.nl (A.H. van Zuijlen).

https://doi.org/10.1016/j.compfluid.2025.106647
Received 19 July 2024; Received in revised form 20 February 2025; Accepted 17 April 2025
Available online 2 May 2025

Flow situation	Fluidelastic instability	Periodic shedding	Turbulence excitation	Acoustic resonance
Axial flow				
Internal				
Liquid	*	—	**	***
Gas	*	—	*	***
Two-phase	*	—	**	*
External				
Liquid	**	—	**	***
Gas	*	—	*	***
Two-phase	*	—	**	*
Cross flow				
Single cylinders				
Liquid	—	***	**	*
Gas	—	**	*	*
Two-Phase	—	*	**	—
Tube Bundle				
Liquid	***	**	**	*
Gas	***	*	*	***
Two-phase	***	*	**	—

***Most important.
**Should be considered.
*Less likely.
—, Does not apply.

Steam generator
Fuel rods
Steam generator and fuel rods

Fig. 1. Vibration excitation mechanisms.
Source: Amended from [15].

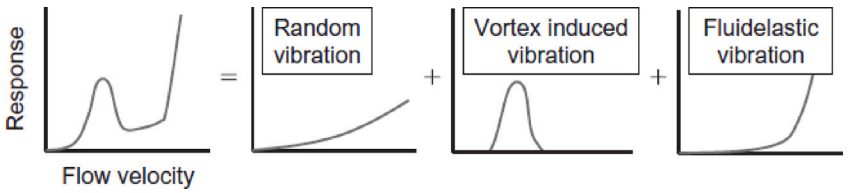

Fig. 2. Vibrational response as a superimposition of different FIV mechanisms [16].

Different parts of the nuclear facility can vibrate due to entirely different excitation mechanisms. This depends on whether the flow is axial or perpendicular and if the fluid is single-phase or multi-phase. Pettigrew et al. [15] provides 4 classifications of FIV mechanisms in nuclear applications. Fig. 1 relates these vibration excitation mechanisms to different flow situations in nuclear reactor applications and gives their relative importance. The current study places importance on capturing Vortex-Induced Vibrations (VIV) that occur due to the periodic wake shedding excitation mechanism.

Fig. 2 reveals how these mechanisms may be superimposed to get the vibrational response from a structure. VIV has a more devastating effect in the lock-in regime while random vibrations or Turbulence-Induced Vibrations (TIV) are present in the entire range of flow velocities with its detrimental effect increasing with flow velocity. The contributions of TIV are also considered in the current study.

With the advancements in Computational Fluid Dynamics (CFD) and Computational Structural Mechanics (CSM), 'coupled CFD-CSM', or 'FSI' solvers are made use of to predict FIV. For VIV, in particular, variations of a cylinder subjected to cross-flow are popular in literature for testing these FSI solvers. They could be for a single elastically mounted cylinders such as in the works of Dobrucali & Kinaci [17] and Martini et al. [18], a pair of such cylinders such as in the work of Ding et al. [19] or for an array of cylindrical tubes such as in the works of Ding et al. [20], Wang. et al. [21], Vivaldi & Baccou [22] and Benhamadouche & Benguigui [23].

In particular, FSI calculations must determine forces which act at both the hydrodynamic frequency and the natural frequency of the structure. The complexity of calculations is determined by the problem of separating physical instability in the flow from numerical errors. Therefore, development of recommendations and further update of the *Best Practice Guidelines* [24] on carrying out the coupled calculations appears to be a relevant problem.

In order to deal with this problem, the Working Group on the Analysis and Management of Accidents (WGAMA) of the OECD/NEA proposed a benchmark [25], based on the complete set of experimental campaigns realized with the work of Bolshukhin et al. [26], that provides the possibility of joint measurements of the vibration and flow hydrodynamic parameters. The benchmark [25] was set up in 2 phases: open and blind. The problem defined for both phases is cross-flow across two in-line cantilevered cylinders with different cylinder sizes for each phase. For each phase, two inflow velocities were simulated: an off-resonance case and a peak resonance case. The open phase results were provided to the benchmark participants apriori for calibration purposes while the blind phase results were disclosed after all calculations were handed in.

This article presents the numerical simulations of both phases considered in the framework of this benchmark. On account of the availability of comprehensive experimental results, the novelty of the current study is the detailed assessment of the numerical results with respect to coupled fluid and structure behaviours. Upon assessing the performance of a CFD approach in reproducing specific flow physics, such as shedding frequency and its harmonics, velocity profiles, acceleration and velocity spectra, etc., it is possible to quantitatively evaluate its impact on structural vibration. This would in turn shed light on the weaknesses of the numerical approach that could be improved on in the future. One such example that would be discussed later in detail is the prediction of the turbulent spectra. By just respecting the best practice guidelines for a numerical simulation, it is difficult to state whether or not the obtained turbulent spectra is resolved "well" or "well-enough". However, knowing the desired results from the experiment

and being able to formally assess the extent to which the predicted spectra match those of the experiment, allows one to quantify the degree of precision required for the simulations. This was either not or rather only partially achieved by previous studies such as in the work of Vivaldi & Baccou [22] and Benhamadouche & Benguigui [23], owing to the lack of high-grade experimental results.

The current study thus aims to present numerical FSI predictions for this benchmark using Unsteady Reynolds Averaged Navier–Stokes (URANS) turbulence models available in the commercial code Simcenter STAR-CCM+ (V2020.3.1). The rationale for this choice over a higher resolution approach such as Detached Eddy Simulations (DES) or Large Eddy Simulations (LES), which are expected to give better frequency response predictions, comes from broadly two reasons. The first reason is the high computational cost incurred for the latter approaches as the grid resolution needs to be sufficiently refined in order to capture the finer turbulent structures present in the flow. The second reason comes from the fact that VIV of cylinders are accompanied by vortices shed at a fixed frequency behind it. Such unsteadiness, i.e, the contribution of coherent modes to the flow dynamics (i.e., frequencies far lower than those of the turbulent fluctuations), may be consistently captured by URANS approaches provided that the flow phenomena of interest have a time scale larger than the time step size. As a consequence of correctly capturing the shed vortices, the resulting VIV is also expected to be captured well. This has also been found in literature regarding the predictions of the 2-equation URANS model of VIV characteristics in turbulent flow around a circular cylinder [27–31] and is thus used in the current study.

In a previous study by the authors [27], the flow around an elastically mounted cylinder subjected to VIV was simulated using a URANS approach. In particular, the FSI solver available in STAR-CCM+ was validated and a total of 7 turbulence models were tested, based on which, 3 turbulence models are shortlisted for testing in the open phase, namely [32]:

- QKW → K-ω SST: QCR (Quadratic Constitutive Relationship)
- QKWT → K-ω SST: QCR + GRT (γ-Re_θ) transition
- CKE → Standard K-ϵ Low Re: Cubic Constitutive Relationship

where 1 model will be selected for the blind phase. By testing the open phase, the capability of URANS in capturing VIV is already revealed along with the best model choice. Based on the shortcomings of the results, a few hypotheses are formulated about the specific cause of difference. These hypotheses are tested and confirmed with the help of the blind phase.

The article is organized as follows: The governing equations and relevant expressions are introduced in Section 2. The experimental setup and parameters of interest for both open and blind phases are provided in Section 3. The numerical setup and results obtained for the open phase are provided in Section 4 while those for the blind phase are provided in Section 5. The conclusions and recommendations for future work are provided in Section 6.

2. Governing equations

Every numerical simulation is based on a mathematical model that tries to describe the physics of the phenomenon being studied. When considering Fluid Structure Interaction, this involves the equations governing the fluid domain, the structural domain and the ways to couple them both. This section provides a brief overview of the equations governing structural mechanics and fluid dynamics with its associated turbulence modelling. Readers who are interested in the finer details of any of the following equations are referred to the STAR-CCM+ user guide [32].

The frame of reference of all FSI simulations in this study use the Lagrangian approach for the solids while using the Arbitrary Lagrangian Eulerian (ALE) approach for the fluid which allows to move the frame of reference independent of the material motion. This method brings together the best of both the Eulerian and Lagrangian approaches by following the motion of the material at the fluid structure interface in a Lagrangian way, while the computational mesh in the interior can be moved arbitrarily to optimize the shape of the elements. In this frame of reference, the velocity in the governing equations becomes relative to the deforming mesh.

2.1. Solid mechanics

If the position of a material point in the undeformed configuration is $\mathbf{X}$, and the displacement of this point to the deformed configuration is $\mathbf{u}(\mathbf{X}, t)$, the position of the material point in the deformed configuration is:

$$\mathbf{x}(\mathbf{X}, t) = \mathbf{X} + \mathbf{u}(\mathbf{X}, t) \tag{1}$$

In component form, the displacement can be expressed as:

$$\mathbf{u} = \begin{bmatrix} u_x & u_y & u_z \end{bmatrix}^T \tag{2}$$

The displacement field of a deformable body is defined by the set of displacement vectors of its material points.

The stress at a point is the force per unit area, as the area over which the force is applied approaches zero. At a point, the state of stress is completely defined by the stress vectors that are associated with three mutually perpendicular planes passing through the point. The state of stress at any point, on any plane, is defined by a second-order tensor of the following form. This is the Cauchy stress:

$$\underline{\sigma} = \begin{bmatrix} \sigma_{xx} & \sigma_{xy} & \sigma_{xz} \\ \sigma_{yx} & \sigma_{yy} & \sigma_{yz} \\ \sigma_{zx} & \sigma_{zy} & \sigma_{zz} \end{bmatrix} \tag{3}$$

Strain is a measure of the deformation of a body in terms of the relative displacement of its material points. Consider two material points in a body that deforms from an initial configuration to some deformed configuration. In 3D, the state of strain at any point in a body is fully described by a second-order symmetric tensor:

$$\underline{\epsilon} = \begin{bmatrix} \epsilon_{xx} & \epsilon_{xy} & \epsilon_{xz} \\ \epsilon_{yx} & \epsilon_{yy} & \epsilon_{yz} \\ \epsilon_{zx} & \epsilon_{zy} & \epsilon_{zz} \end{bmatrix} \tag{4}$$

In the current study, the infinitesimal strain approximation is used to describe the elastic behaviour of the cylinders, for which the deformations are expected to be small. The infinitesimal strain is defined as:

$$\underline{\epsilon} = \frac{1}{2}\left(\frac{\partial \mathbf{u}}{\partial \mathbf{X}} + \left[\frac{\partial \mathbf{u}}{\partial \mathbf{X}}\right]^T\right) \tag{5}$$

2.1.1. Governing equations

In the Lagrangian approach, mass is always conserved within the control volume. The mass that is contained in any deformed volume is the same mass that was originally contained in the undeformed volume:

$$M = \int_{V(t)} \rho(t)\, \mathrm{d}V = \int_{V_0} \rho_0\, \mathrm{d}V \tag{6}$$

Since the mass within the volume is conserved, volume changes result in density changes. In fact, this leads to a slightly different interpretation of the material density specified by the user in STAR-CCM+. The specified density is the material density in the undeformed configuration, at a reference temperature.

The motion of a solid body is governed by Cauchy's equilibrium equation, which expresses the conservation of linear momentum for a continuum as given by:

$$\rho\ddot{\mathbf{u}} - \nabla \cdot \underline{\sigma} - \mathbf{b} = 0 \tag{7}$$

where $\mathbf{u}$ is the displacement of the solid body, $\mathbf{b}$ is the total body force per unit volume and $\underline{\sigma}$ is the symmetric Cauchy stress tensor. The above equation is usually accompanied with Dirichlet and Neumann boundary conditions, which in Solid Mechanics jargon are called constraints and loads respectively.

The above equations are discretized after bringing to their weak form using the Finite Element Method. The involved accelerations and velocities can be approximated using a 1st order Backward Euler method or a 2nd order Newmark method, thereby making it possible to solve the governing equations.

2.1.2. Rayleigh damping model

The formulation presented in Eq. (7) does not take into account the damping mechanisms that arise in time-dependent systems such as that in the current study. In dynamic problems, the contribution of damping forces can be taken into account by including a velocity dependent damping term, $c\dot{\mathbf{u}}$, in the equation of motion:

$$\rho\ddot{\mathbf{u}} + c\dot{\mathbf{u}} - \nabla\cdot\underline{\sigma} - \mathbf{b} = 0 \tag{8}$$

which assumes a linear relationship between the damping force and velocity. The weak form of Eq. (8) can be constructed and discretized, leading to the general discretized equation for a linear elastic damped system:

$$\mathbf{M}\ddot{\mathbf{u}}(t) + \mathbf{C}\dot{\mathbf{u}}(t) + \mathbf{K}\mathbf{u}(t) = \mathbf{f}^{ext} \tag{9}$$

As damping is a complex combination of different phenomena, the damping matrix is often approximated using Rayleigh damping, which models the damping matrix as a linear combination of the stiffness and mass matrices:

$$\mathbf{C} = \tau_K\mathbf{K} + f_M\mathbf{M} \tag{10}$$

The scalar coefficients τ_K and f_M can be determined from a desired modal damping factor and the knowledge of the first two eigenfrequencies of the undamped system. An even simpler choice, as used in the current study, is to restrict the Rayleigh damping to stiffness proportional damping, by assuming $f_M = 0$ and $\tau_K > 0$, and tune the parameter with the fundamental eigenfrequency:

$$\tau_K = \frac{2\zeta}{\omega} \tag{11}$$

2.2. Fluid mechanics

In this section, the key equations governing fluid flow are introduced along with the associated turbulence and transition modelling.

2.2.1. Governing equations

The governing equations of fluid flow, also called the *Navier–Stokes Equations*, over a finite control volume can be written in an integral sense (conservation form). This follows the approach of the Finite Volume Discretization. URANS turbulence models provide closure relations for the Reynolds-Averaged Navier–Stokes equations, that govern the transport of the mean flow quantities. The obtain the URANS equations, each solution variable ϕ in the instantaneous Navier–Stokes equations is decomposed into its mean, or averaged, value $\overline{\phi}$ and its fluctuating component ϕ':

$$\phi = \overline{\phi} + \phi' \tag{12}$$

where ϕ represents velocity components, pressure or energy. This gives the equations for the mean quantities:

$$\begin{aligned}
\frac{\partial\rho}{\partial t} + \nabla\cdot(\rho\overline{\mathbf{v}}) &= 0\\
\frac{\partial}{\partial t}(\rho\overline{\mathbf{v}}) + \nabla\cdot(\rho\overline{\mathbf{v}}\otimes\overline{\mathbf{v}}) &= -\nabla\cdot\overline{p}\mathbf{I} + \nabla\cdot(\overline{\mathbf{T}} + \mathbf{T}_{RANS}) + \mathbf{f}_b\\
\frac{\partial}{\partial t}(\rho\overline{E}) + \nabla\cdot(\rho\overline{E}\overline{\mathbf{v}}) &= -\nabla\cdot\overline{p}\,\overline{\mathbf{v}} + \nabla\cdot(\overline{\mathbf{T}} + \mathbf{T}_{RANS})\overline{\mathbf{v}} - \nabla\cdot\overline{\mathbf{q}} + \mathbf{f}_b\cdot\overline{\mathbf{v}}
\end{aligned} \tag{13}$$

where the terms are as described earlier with the exception of a new term: the stress tensor $\mathbf{T}_{RANS}$ which is given by

$$\mathbf{T}_{RANS} = \rho\begin{bmatrix}\overline{u'u'} & \overline{u'v'} & \overline{u'w'}\\ \overline{v'u'} & \overline{v'v'} & \overline{v'w'}\\ \overline{w'u'} & \overline{w'v'} & \overline{w'w'}\end{bmatrix} + \frac{2}{3}\rho k\mathbf{I} \tag{14}$$

where k is the turbulent kinetic energy. In the current study, the Eddy Viscosity models are employed to model $\mathbf{T}_{RANS}$ in terms of the mean flow quantities via the turbulent eddy viscosity μ_t, and hence provide closure of the governing equations. The most common model is known as the Boussinesq approximation:

$$\mathbf{T}_{RANS,L} = 2\mu_t\mathbf{S} - \frac{2}{3}(\mu_t\nabla\cdot\overline{\mathbf{v}})\mathbf{I} \tag{15}$$

where $\mathbf{S}\frac{1}{2}(\nabla\overline{\mathbf{v}}+(\nabla\overline{\mathbf{v}})^T)$ is the mean strain rate tensor which uses the mean velocity, $\overline{\mathbf{v}}$ in its formulation. Another important term that is later used is the mean vorticity tensor $\mathbf{W} = \frac{1}{2}(\nabla\overline{\mathbf{v}} - \nabla\overline{\mathbf{v}}^T)$. The popular k-ϵ and k-ω SST models are employed in the current study that solve additional transport equations for scalar quantities that enable the derivation of μ_t. Note that the stress tensor T_{RANS} finally used in the momentum equation will be the sum of $T_{RANS,L}$, defined above and $T_{RANS,NL}$ defined based on the constitutive relationship chosen for a given model.

K-ϵ Model

The K-Epsilon turbulence model is a two-equation model that solves transport equations for the turbulent kinetic energy k and the turbulent dissipation rate ϵ in order to determine the turbulent eddy viscosity. In particular, the Low-Reynolds Number variation of the model by Lien et al. [33] is made use of. This is done in STAR-CCM+ by applying damping functions to some of the coefficients (C_μ, $C_{\epsilon 2}$) in the model. The turbulent eddy viscosity μ_t is calculated as:

$$\mu_t = \rho C_\mu f_\mu k T \tag{16}$$

where T is the turbulent time scale which, for the 'Realizable' option, is given by:

$$T = \max\left(\min\left(\frac{k}{\epsilon}, \frac{C_T}{C_\mu f_\mu S}\right), C_t\sqrt{\frac{\nu}{\epsilon}}\right) \tag{17}$$

where ν is the kinematic viscosity, S is the modulus of the mean strain rate tensor ($S = |\mathbf{S}| = \sqrt{2\mathbf{S}:\mathbf{S}}$). The transport equations for the kinetic energy k and the turbulent dissipation rate ϵ are:

$$\begin{aligned}
\frac{\partial}{\partial t}(\rho k) + \nabla\cdot(\rho k\overline{\mathbf{v}}) &= \nabla\cdot\left[\left(\mu + \frac{\mu_t}{\sigma_k}\right)\nabla k\right] + P_k - \rho\epsilon + S_k\\
\frac{\partial}{\partial t}(\rho\epsilon) + \nabla\cdot(\rho\epsilon\overline{\mathbf{v}}) &= \nabla\cdot\left[\left(\mu + \frac{\mu_t}{\sigma_\epsilon}\right)\nabla\epsilon\right] + \frac{\epsilon}{k}C_{\epsilon 1}P_\epsilon - C_{\epsilon 2}f_2\rho\frac{\epsilon^2}{k} + S_\epsilon
\end{aligned} \tag{18}$$

For the chosen 'Standard K-ϵ Low Re' model of STAR-CCM+ with the Yap correction [34], the production terms are given by

$$\begin{aligned}
P_k &= G_k + G_{nl} + G_b - Y_M\\
P_\epsilon &= G_k + G_{nl} + G' + C_{\epsilon 3}G_b + \frac{\rho}{C_{\epsilon 1}}Y'_y
\end{aligned} \tag{19}$$

where G_k is the turbulent production, G_{nl} is the nonlinear production, G_b is the buoyancy production, G' is the additional production, Y_M is the compressibility modification and Y'_y is the Yap Correction [34]. By default, the Boussinesq approximation implies a linear constitutive relation. Nonlinear constitutive relations [33] account for anisotropy of turbulence by adding nonlinear functions of the strain and rotation tensors. The available relations are tabulated in Table 1.

K-ω SST Model

The K-Omega turbulence model is a two-equation model that solves transport equations for the turbulent kinetic energy k and the specific dissipation rate ω, the dissipation rate per unit turbulent kinetic energy ($\omega \propto \frac{\epsilon}{k}$), in order to determine the turbulent eddy viscosity. In this model, the turbulent eddy viscosity μ_t is calculated as:

$$\mu_t = \rho k T \tag{20}$$

Table 1
Constitutive relations [32].

Constitutive relation	Formulation	Where:
Quadratic (QCR)	$\mathbf{T}_{RANS,NL} = -4\mu_t \frac{k}{\epsilon}\left\{C_1\left[S\cdot S - \frac{1}{3}I(S:S)\right] + C_2(W\cdot S + S\cdot \mathbf{W}^T) + C_3\left[W\cdot \mathbf{W}^T - \frac{1}{3}I(W:\mathbf{W}^T)\right]\right\}$	$C_1 = \frac{C_{NL1}}{(C_{NL6}+C_{NL7}\overline{S}^3)C_\mu}$ $C_2 = \frac{C_{NL2}}{(C_{NL6}+C_{NL7}\overline{S}^3)C_\mu}$ $C_3 = \frac{C_{NL3}}{(C_{NL6}+C_{NL7}\overline{S}^3)C_\mu}$
Cubic	$\mathbf{T}_{RANS,NL} = \mathbf{T}_{RANS,quad} - 8\mu_t \frac{k^2}{\epsilon^2}\{C_4[(S\cdot S)\cdot W + \mathbf{W}^T\cdot(S\cdot S)] + C_5(S:S - W:\mathbf{W}^T)\left[S - \frac{1}{3}\mathrm{Tr}(S)I\right]\}$	$\mathbf{T}_{RANS,quad}$ is the QCR formulation of $\mathbf{T}_{RANS,NL}$, $C_4 = C_{NL4}C_\mu^2$ $C_5 = C_{NL5}C_\mu^2$

where T is the turbulent time scale which when calculated using the Durbin's realizability constraint [35] is given by:

$$T = \min\left(\frac{1}{\max(\omega/\alpha^*, (SF_2)/a_1)}, \frac{C_T}{\sqrt{3}S}\right) \tag{21}$$

The transport equations for the kinetic energy k and the specific dissipation rate ω are:

$$\begin{aligned}\frac{\partial}{\partial t}(\rho k) + \nabla\cdot(\rho k\overline{\mathbf{v}}) &= \nabla\cdot\left[\left(\mu + \mu_t\sigma_k\right)\nabla k\right] + P_k - \rho\beta^*\omega k + S_k\\ \frac{\partial}{\partial t}(\rho\omega) + \nabla\cdot(\rho\omega\overline{\mathbf{v}}) &= \nabla\cdot\left[\left(\mu + \mu_t\sigma_\omega\right)\nabla\omega\right] + P_\omega - \rho\beta\omega^2 + S_\omega\end{aligned} \tag{22}$$

For the chosen K-Omega SST Model, the production terms are given by:

$$\begin{aligned}P_k &= G_k + G_{nl} + G_b\\ P_\omega &= G_\omega + D_\omega\end{aligned} \tag{23}$$

where G_k, G_{nl} and G_b are the same terms used in the K-ϵ model, G_ω is the specific dissipation production and D_ω is the cross-diffusion term. For the QCR relation used in this study:

$$\begin{aligned}T_{RANS,NL} &= -2\mu_t 0.04645(\mathbf{O}\cdot\mathbf{S} - \mathbf{S}\cdot\mathbf{O})\\ \mathbf{O} &= \frac{\mathbf{W}}{\sqrt{(\mathbf{S}-\mathbf{W})(\mathbf{S}-\mathbf{W})}}\end{aligned} \tag{24}$$

As for the use of a transition model, the γ-Re_θ model [36,37] is used in the current study, which solves for two additional transport equations in addition to the two-equation K-ω SST model. The model was incomplete, as published, since two critical correlations were proprietary and hence omitted. A justification for such an omission is that the model provides a framework for users to implement their own correlations. In the current study, the default correlations implemented by STAR-CCM+ are used. Without providing intricate details of the involved terms, the intermittency, γ, and transition momentum thickness Reynolds number, $\overline{Re_{\theta t}}$, transport equations are given below:

$$\begin{aligned}\frac{\mathrm{d}}{\mathrm{d}t}(\rho\gamma) + \nabla\cdot\rho\gamma\overline{\mathbf{v}} &= \nabla\cdot\left[\left(\mu + \frac{\mu_t}{\sigma_f}\right)\nabla\gamma\right] + P_\gamma - E_\gamma\\ \frac{\mathrm{d}}{\mathrm{d}t}(\rho\overline{Re_{\theta t}}) + \nabla\cdot(\rho\overline{Re_{\theta t}}\overline{\mathbf{v}}) &= \nabla\cdot[\sigma_{\theta t}(\mu+\mu_t)\nabla\overline{Re_{\theta t}}] + P_{\theta t} + D_{SCF}\end{aligned} \tag{25}$$

where $\sigma_f = 1$ and $\sigma_{\theta t} = 2$ are model constants, P_γ and $P_{\theta t}$ are production terms, E_γ is the destruction term and D_{SCF} is the cross flow term.

3. Experimental setup

The test facility is located at the JSC "Afrikantov OKBM" in Russia. The experimental setup features a rectangular flow channel of dimensions 550 × 200 × 30 mm^3 containing two in-line cylinders in cross flow. The general view of the model installed in the test facility and the schematic of the test section are shown in Fig. 3. The basic hydrodynamic process observed behind the two in-line cylinders, exposed to the cross flow, is a vortex street with a repetitive structure (Karman vortex street) and vortex shedding frequency f_s. It is accompanied by the excitation of the structure at the f_s frequencies and at the natural frequencies f_n.

Table 2
Open phase: structural properties [25].

Structure	Material	Density, ρ_s (kg/m^3)	Young's modulus, E (GPa)	Poisson's ratio, ν
Bobs for Cylinder1	Brass	9450	200	0.33
Bobs for Cylinder2	Brass	12 450	200	0.33

The hollow cylinders in the experiment have equal diameters, are flexible and have a cantilever attachment. Two types of cylinders were manufactured depending on the phase of study as can be seen in the schematics of Fig. 4:

1. Open Phase: The hollow stainless steel cylinders have a diameter of $D = 7$ mm and wall thickness 0.3 mm. Each cylinder has two brass accelerometer mountings of diameter 6.4 mm and length 12 mm soldered (the length includes the solder deposit) internally at the tip of the cylinder and at near halfway length of the cylinder. The material properties of the resulting structure are given in Table 2.
2. Blind Phase: The hollow stainless steel cylinders have a diameter of $D = 10$ mm and wall thickness 1 mm. Each cylinder has only one brass accelerometer mounting of diameter 8 mm and lengths 14 mm and 29 mm (the lengths do not include the solder deposit), respectively, soldered internally at the tip of the cylinder. The material properties of the resulting structure are provided in Table 3.

The working fluid is water at a reference static pressure of 1 kgf/cm^2 (98.07 kPa) for both phases. For each phase, 2 flow rates were experimentally tested: an off-resonance case and a peak resonance case with respect to Cylinder1. The operating conditions for the open and blind phases are tabulated in Table 4. In the current study, the peak resonance case of the open phase and all cases of the blind phases are numerically simulated.

In the experiment, the natural frequency and structural damping of the cylinders in the channel were analysed for both phases by measuring the vibrations under the impact excitations of the channel and producing a Frequency Response Function (FRF) plot. These tests were repeated for the channel with and without water. The natural frequencies so obtained in air ($f_{n,air}$) and water ($f_{n,water}$) are tabulated in Table 5.

The FRF plots, created based on the experimental results provided for the test of the channel with water, are provided in Fig. 5. Using these plots, the damping ratio (ζ) or its related parameters like the loss factor (η) and quality factor (Q) is found using the 'half-power' or '3 dB' rule [38]. These damping parameters are calculated using:

$$\frac{\Delta f}{f} = \eta = \frac{1}{Q} = 2\zeta\sqrt{1-\zeta^2} \approx 2\zeta \tag{26}$$

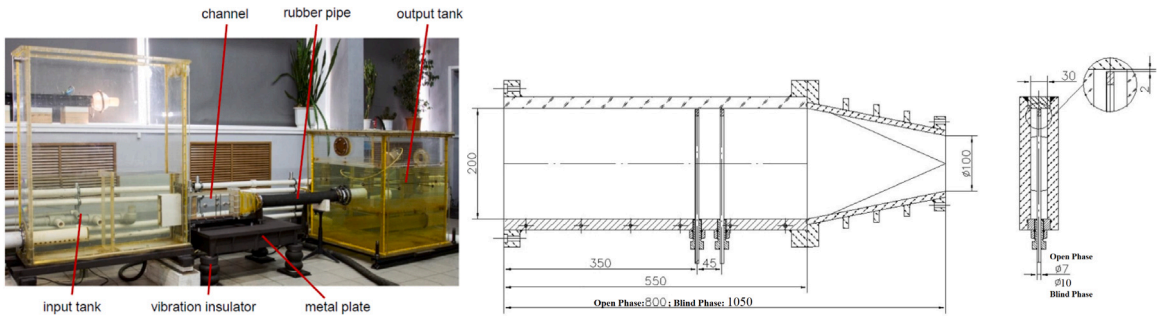

(a) Experimental Setup [26] (b) Schematic of Test Section [25]

Fig. 3. Experimental setup and the schematic of the test section.

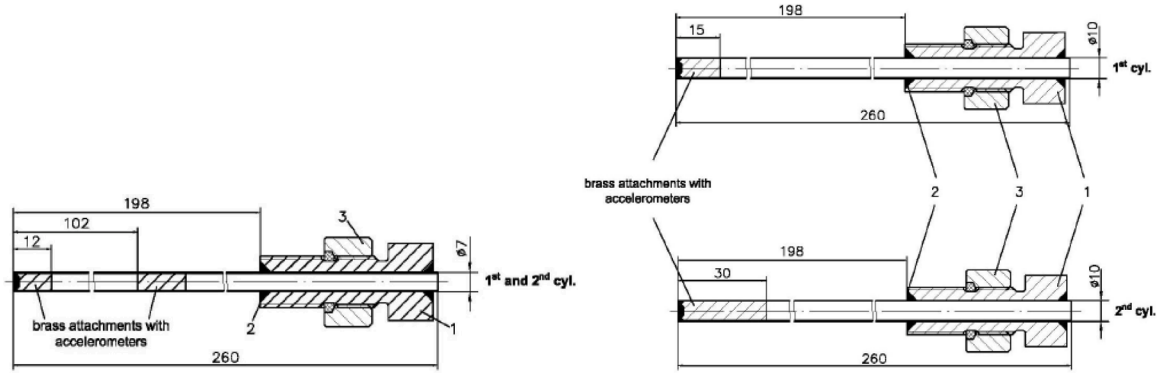

(a) Open Phase (b) Blind Phase

Fig. 4. Schematic of the cylinders [25].

Table 3
Blind phase: structural properties [25].

Structure	Material	Density, ρ_s (kg/m^3)	Young's modulus, E (GPa)	Poisson's ratio, ν
Hollow Cylinders 1 & 2	Stainless Steel	7850	200	0.30
Bob for Cylinder1	Brass	8700	200	0.33
Bob for Cylinder2	Brass	7500	200	0.33

Table 4
Operating conditions [25].

Property	Open phase		Blind phase	
	Off-resonance	Peak resonance	Off-resonance	Peak resonance
Fluid Temperature (° C)	10	10	19	19
Inflow Rate (m^3/h)	10	16	16	35
Re	2477.64	3964.23	7210.96	15 773.96

Table 5
Natural frequencies [25].

Phase	Cylinder1		Cylinder2	
	$f_{n1,air}$ (Hz)	$f_{n1,water}$ (Hz)	$f_{n2,air}$ (Hz)	$f_{n2,water}$ (Hz)
Open	107.0	98.0	98.0	90.0
Blind	183.9	164.9	168.8	153.0

where Δf is the width of the FRF curve 3 dB below the peak at frequency f. The loss factor for both cylinders vibrating in water comes out to $\eta = 0.016$ for the open phase and $\eta = 0.007$ for the blind phase. The approximation $\zeta = 0.5\eta$ is accurate within 5E-3% for $\eta \in [0, 0.02]$ and is thus made use of giving $\zeta = 0.008$ for the open phase and $\zeta = 0.0035$ for the blind phase. These values are later used in conjunction with the values from the numerical structural tests to provide structural damping for the FSI tests using the Rayleigh Damping model as discussed in Section 2.1.2.

During testing, dynamic parameters were measured correspondingly by different systems. The experimental data were registered as a function of time. The following measurements were performed for both phases:

- $v(t)$ – time oscillation of velocity pulsations
- $p(t)$ – time oscillation of pressure pulsations on the channel wall
- $a(t)$ – time oscillation of cylinders' vibration acceleration

Fig. 6 shows the locations of the measurement points. A coordinate system is used where X-axis is directed along the channel (drag-direction), Y-axis is directed across the channel in the horizontal plane (lift-direction), and Z-axis is directed along the cylinders in the vertical

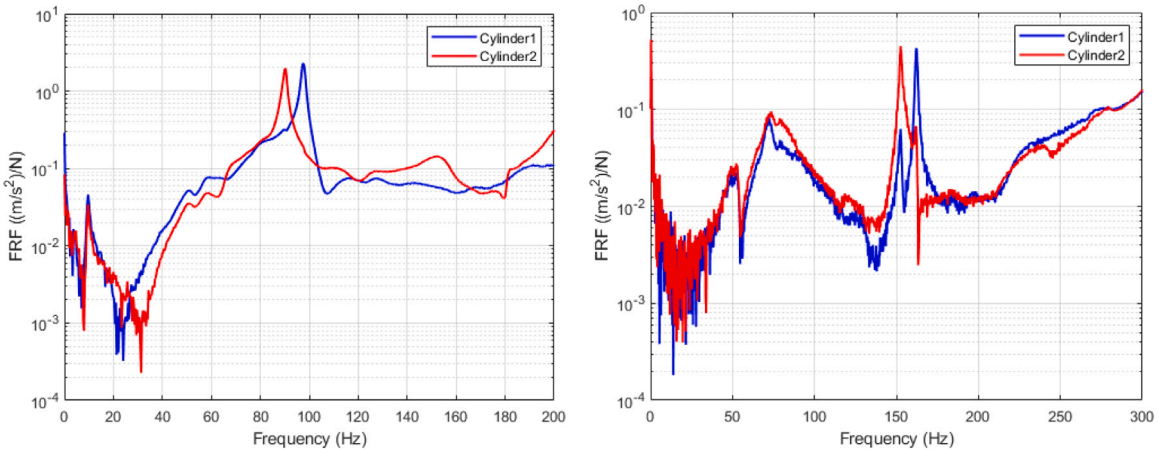

(a) Open Phase (b) Blind Phase

Fig. 5. FRF curves for the two cylinders under impact excitation of the channel with water.

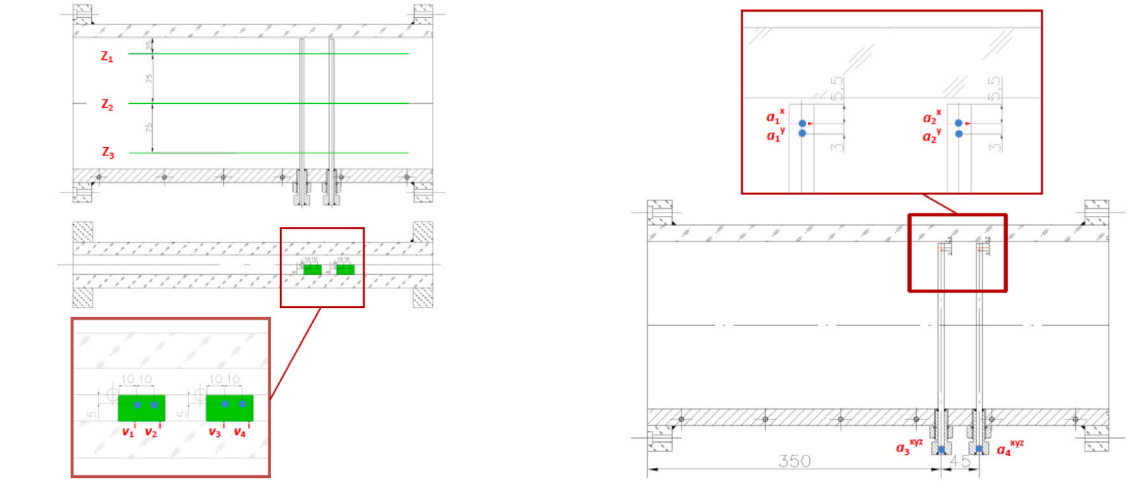

(a) Locations of Velocity Pulsations Measurements in the i^{th} Plane (b) Locations of Cylinders' Vibration Acceleration Measurement

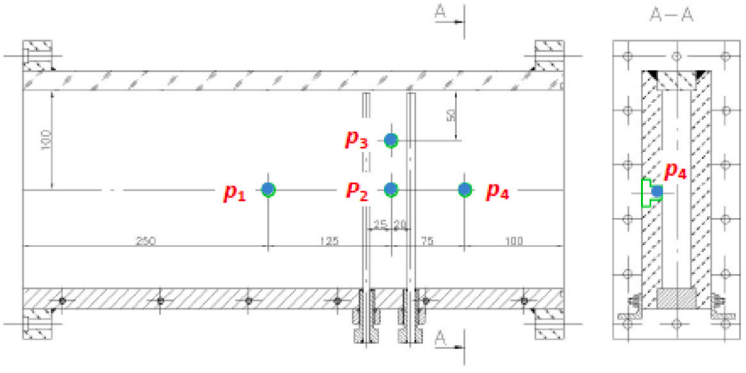

(c) Locations of Pressure Pulsations Measurements

Fig. 6. Location of measurement points for different parameters [25,26].

plane. Given that the numerical model constraints the ends of the cylinders to the channel wall perfectly, the accelerometer readings of a_3^{xyz} and a_4^{xyz} (see Fig. 6(b)) are not made use of. The Power Spectral Density (hereinafter - spectrum) of velocity and pressure pulsations, as well as vibration accelerations are later calculated based on the time series.

Besides measurements at the above locations, horizontal velocity profile measurements were made 10 mm and 20 mm behind the

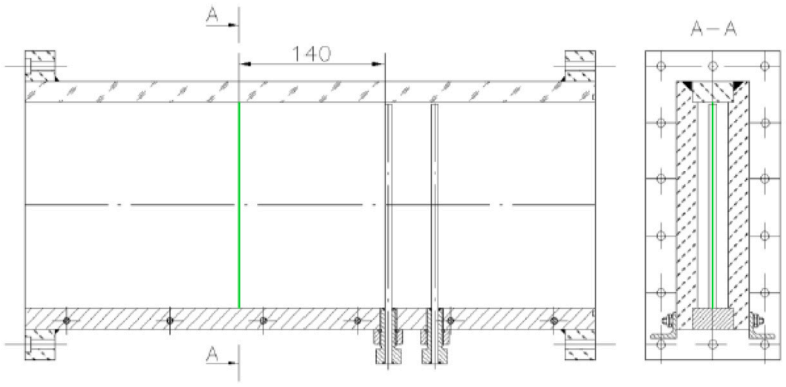

(a) Vertical Plane

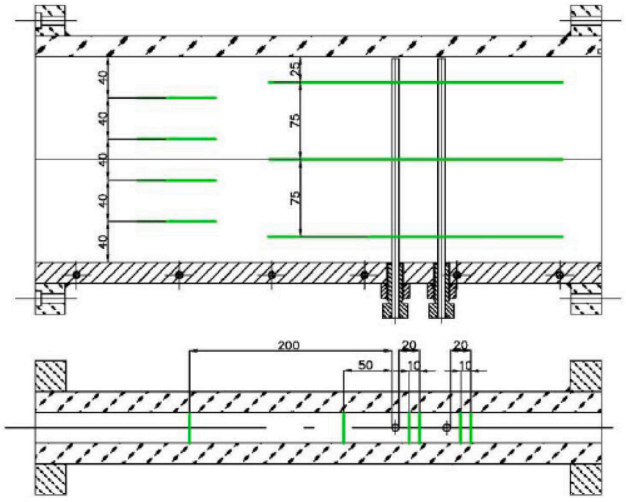

(b) Horizontal Planes

Fig. 7. Locations of velocity profiles measurement in the vertical and horizontal planes [25,26].

cylinders as shown in Fig. 7(b). Furthermore, to aid in selecting inlet flow conditions, additional velocity profile measurements were made. These measurements were performed in the following sections and are shown in Fig. 7:

- Average and Root Mean Squared (RMS) profile in the vertical plane of longitudinal velocity $V_x(z)$ in front of the 1st cylinder at a distance of 140 mm
- Average and RMS profile in four horizontal planes (40, 80, 120 and 160 mm) of longitudinal velocity $V_x(y)$ in front of the 1st cylinder at a distance of 200 mm
- Average and RMS profile in three horizontal planes (25, 100 and 175 mm) of longitudinal velocity $V_x(y)$ in front of the 1st cylinder at a distance of 50 mm

4. Open phase

In this section, the open phase of the benchmark is discussed. The numerical setup is provided in Section 4.1, the results are provided and discussed in Section 4.2, where the hypotheses to be tested in the blind phase are formulated.

4.1. Numerical setup

For the simulation domain, only the rectangular flow channel of the experimental test section (and its contents) are considered as shown in Fig. 8. The problem is set up in STAR-CCM+ as follows: For the fluid, the incompressible finite-volume URANS solver is selected along with a SIMPLE scheme approach for solving the pressure and velocity equations in a segregated way. A 2nd order upwind spatial convection scheme is chosen along with a 2nd order implicit time integration scheme. The pressure and velocity equations are given underrelaxation

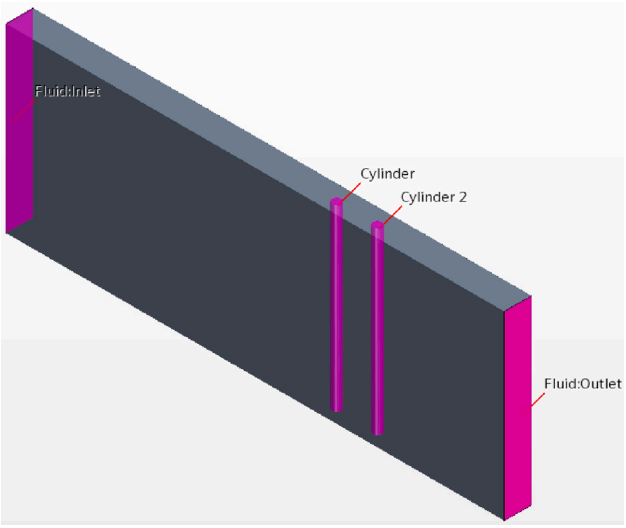

Fig. 8. Simulation domain.

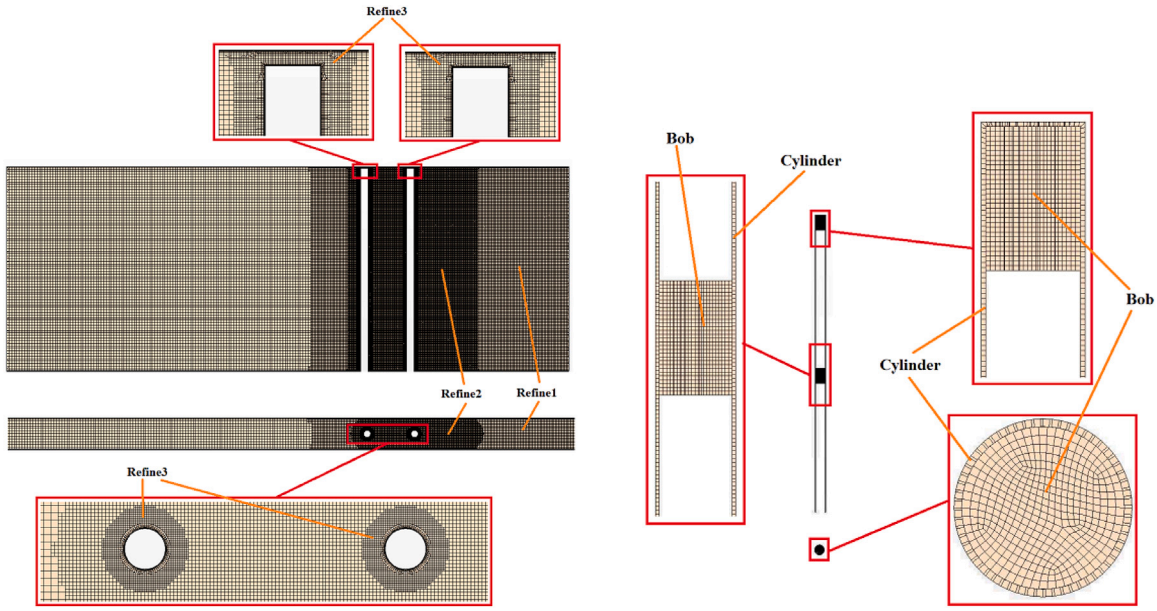

(a) Fluid Mesh (b) Structural Mesh

Fig. 9. Sectional views of the meshes.

(UR) factors of 0.2 and 0.6, respectively. The four channel walls and the exposed cylinder surfaces are prescribed a no-slip boundary condition. A reference pressure of 98.07 kPa is prescribed for the fluid and a constant gauge pressure of 0 Pa is prescribed for the outlet. For the inlet, a time-varying uniform velocity is prescribed for the FSI study as given by:

$$u(0,y,z,t) = \begin{cases} u(0,y,z)\frac{1-\cos\left(\frac{\pi}{T}t\right)}{2}, & \text{if } t < T \\ u(0,y,z), & \text{otherwise} \end{cases} \quad (27)$$

$$u(0,y,z) = 0.74 \text{ m/s}, \quad T = 1.0 \text{ s}$$

This cosine ramped profile is chosen over suddenly applying the velocity at the inlet for the numerical stability of the FSI solver. The cosine ramp is expected to be even more suitable than a standard linear ramp based on the first derivative of the profiles. The resulting acceleration profile would have sudden jumps at the beginning and end of the linear velocity ramp while it would be smooth for the cosine velocity ramp.

For the solid, the finite-element solver is selected that solves for structural displacements and thereby calculates strains and stresses. The 2nd order Newmark implicit integration scheme (Newmark parameter, $\gamma = 0.5$) is employed to solve dynamic displacements. At this point, a choice is to be made between the infinitesimal strain and finite strain approximations. The expected displacements in both streamwise (x) and cross flow (y) directions are less than 1 mm which, relative to the 198 mm length of the cylinders, is less than 0.51% of the cylinder length. Furthermore, displacements and accelerations in the axial direction (z) are not measured in the experiment. Thus, it seems suitable to apply the infinitesimal strain approximation. For the boundary condition, the annular surfaces at the bottom of the cylinders are grounded while the outer wetted surfaces are declared as an FSI interface. Internally, the brass bobs are fixed in their relative positions using the bonded boundary condition between the bob curved surface and the cylinder inner curved surface. For the FSI coupling, a UR factor of 0.5 is prescribed.

The fluid mesh is created using the 'Automatic Mesh' functionality of STAR-CCM+. For the fluid, a hexahedral mesh is created with three volume refinements. The volume refinements starting upstream Cylinder1 are situated around the cylinders and also in the wake of the cylinders. This arrangement of volumetric refinements comes from a pure CFD analysis of 3 candidate meshes [39]. Approaching the cylinder from the inlet by crossing each refinement region reduces the target base size of 2.5 mm by half sequentially. To ensure good transition between the refinement regions, a growth rate of 1.1 is selected. Prism layers are setup on all no-slip walls with a wall y^+ of 1. The fluid mesh is shown in Fig. 9(a) with a cell count of 7.05M cells. For the FSI simulations, the 'B-Spline' mesh morpher is selected.

For the solid, unstructured meshes are set up for the cylinders and their internal bobs. The mesh for the cylinders are quad dominant with one element in the thickness, having a total cell count of about 69k for each cylinder. The bobs are filled with a quad dominant mesh with 30 layers each, having a total cell count of 12k for each bob. Sectional views of the solid mesh are shown in Fig. 9(b). For low computational effort, linear finite elements are employed.

Before proceeding to the FSI simulations, there is a need to fine tune the structures to the experimental vibrational frequencies. For the experimental study, it was mentioned that the brass bobs were 12 mm in length including the solder which is lesser in density compared to brass. Furthermore, the cylinders had additional length that ran into the wall of the channel which was then fixed by a tightening nut arrangement. This and the fact that there is no accelerometer equipment (which has its own mass) in the numerical setup, calls for fine tuning the structural model. This was done by altering the length of the bobs. Numerically testing the vibrations of select cylinder model candidates in vacuum and water, the final choice is made to proceed with a bob length of 10 mm. The results for different choices of bob length are shown in Tables 6 and 7.

The last item for the FSI setup is the mismatch in structural damping. There appeared to be a significant gap in the prediction of the damping ratio in the vibration test in water even for the optimal bob length of 10 mm. This is remedied by adding structural damping via the aforementioned 'Rayleigh Damping' model. The difference between the damping calculated for vibration test in water and the expected value is used for calculating the stiffness proportional damping constant as per Eq. (11). With this, all relevant parameters for the FSI study are finalized and the results obtained for the same are discussed in the following subsection.

4.2. FSI study

The FSI study is carried out for the peak resonance case of 0.74 m/s inflow using the aforementioned turbulence models QKW, QKWT and

Table 6
Results for Vibration Tests in Vacuum.

Bob Length (mm)	Natural frequency (Hz)	
	Cylinder1	Cylinder2
12.0	104.28	96.06
11.0	106.95	98.04
10.5	107.82	99.50
10.0	108.69	100.33
Exp.	107.00	98.00
Soln.		

Table 7
Results for vibration tests in water.

Bob Length (mm)	Natural frequency (Hz)		Damping ratio	
	Cylinder1	Cylinder2	Cylinder1	Cylinder2
12.0	90.09	84.33	0.0056	0.0041
11.0	94.34	88.49	0.0064	0.0048
10.5	95.69	88.88	0.0065	0.0048
10.0	96.62	90.09	0.0065	0.0049
Exp.	98.00	90.00	0.0080	0.0080
Soln.				

CKE, which were shortlisted from a previous work on VIV of a single cylinder [27]. To keep the FSI coupling stable during the start up of the simulation, a cosine ramping of the inflow velocity is given for 1 s (1.347 Flow Passes [FP]) as per Eq. (27). A total simulation time of 7 s (9.428 FP) is provided. To adhere to the 100 sampling point thumb rule, a time step of 0.4 ms is used during the cosine ramping and is reduced to 0.36 ms for the remainder of the simulation. Using the back-windowing approach on the created spectra plots, it was found that transient results lasted roughly a flow pass after the end of the cosine ramping period. Thus, only the results from 1.75 s to 7 s, or the last 7.071 FP, are used for creating the spectra. Before presenting the main results, the issue of inflow turbulence is addressed.

4.2.1. Inflow turbulence

The value of inflow turbulence intensity was not formally specified in the experiment. This was left to be deduced from the mean and RMS velocity profiles provided at locations listed in Section 3. For making the selection, the vertical profile 140 mm ahead of Cylinder1 is consulted. Based on the experimental data shown in Fig. 10, a turbulence intensity of 4.95% was predicted by the PIV measurements while a value of 1.71% was predicted by LDV. Given the lower experimental measurement error of LDV (1%) compared to PIV (3%–4%) and the inherent superior temporal resolution of the LDV technique, the aim is to obtain good agreements with the LDV results at this location. To do so, the ratio of turbulent kinetic energy at the inlet to that at this location was estimated from a pure CFD simulation. Assuming similar dissipation for the FSI study for all 3 tested turbulence models and the following relation between turbulent kinetic energy and turbulence intensity, a value of 5% was selected for the inflow turbulence:

$$k = \frac{3}{2}(U_x I_x)^2 \tag{28}$$

where k is the turbulent kinetic energy, U_x is the flow velocity at the location of interest and I_x is the turbulence intensity at the location of interest. Based on this choice of turbulence intensity, the results so obtained by the turbulence models are plotted in Fig. 10. For the mean velocity shown in Fig. 10(a), the simulation results are near overlapping with good agreement (within 5%) with the PIV profile for a large part of the profile away from the walls. The PIV measurements near the walls possibly suffer from laser reflections. The simulation results match well with those of LDV near the walls.

For the RMS fluctuations shown in Fig. 10(b), the simulation results are presented as a quantity resolved by the mesh which captures actual velocity fluctuations and as a quantity modelled through the turbulent kinetic energy as per Eq. (28). Since there are no real turbulent structures introduced at the inlet and the distance from Cylinder1 is rather large, the resolved fluctuations are quite small, ranging from 1.2E−5 m/s at the channel centre to 1E-4 m/s in the boundary layer of the channel walls. The modelled fluctuations, however, are of the same order of magnitude of the experimental data with a better match (within 10%) with the LDV results as intended. While the three models agree well with each other over the majority of the domain, a difference is noted at the peaks near the channel walls which comes from the difference in prediction of k in the boundary layers by the considered models.

A similar agreement of the numerical results to the experimental results were also observed for the mean and RMS profiles at locations 50 mm and 200 mm ahead of Cylinder 1. In the interest of brevity of the article, they are not presented here. Based on the results considered so far, the setting for the inflow turbulence is validated. The following section reveals the primary results of this study which are the pressure, acceleration and velocity spectra and the predicted displacements followed by the secondary results which include the vorticity plots and the velocity profiles aft of the cylinders.

4.2.2. Obtained results

The primary results of interest for the FSI study are the velocity, acceleration and pressure spectra for the points as per Fig. 6. The probe points for the acceleration measurement are also used to track the displacements of the cylinders in their respective drag and lift directions. The pressure spectra plots for the different turbulence models are shown along with the experimental results in Fig. 11. To obtain clean spectra plots, linear averaging is applied with a window size of 30 and 5 for the experimental results and numerical results, respectively. The experimental results show several peaks in the plots. These correspond to the vortex shedding frequency (f_s = 24.4 Hz) and its multiples as well as the natural frequencies of the cylinders (f_{n1} = 98 Hz and f_{n2} = 90 Hz) and its multiples.

Additional peaks labelled by f^* and its multiples are linked with the frequency of the pump. It is observed that the largest peak corresponds to the natural frequency of Cylinder1 which coincides with the 4th harmonic of f_s. Furthermore, this also coincides with the 3rd harmonic of pump frequency. This is not desirable as the synergy with the pump has lead to an overestimated PSD for f_{n1}, something that would not be expected from an ideal inlet used in the simulation.

The numerical predictions differ appreciably based on the turbulence model selected. The overall trend of decreasing spectral density with increasing frequency is captured well by the FSI results. However, not all peaks are clearly identified. For P_1, which lies upstream of Cylinder1, only the even harmonics of f_s are distinct. For P_2 and P_3, which lie in between the cylinders, only the first harmonic and even harmonics of f_s are distinct. For P_4, which lies downstream of Cylinder2, only the first harmonic of f_s is distinct. These observations imply easier propagation of the frequency pertinent to the streamwise or drag direction (even harmonics) than it is for the cross flow or lift direction (odd harmonics) and that the first harmonic is more easily captured downstream of the source (the cylinders) rather than upstream. In addition, a peak corresponding to the natural frequency of Cylinder2 (f_{n2}) is predicted at 88 Hz.

Surprisingly, the peak corresponding to the natural frequency of Cylinder1 is not distinctly captured. As mentioned earlier, the pump frequency (f^*) has its third harmonic coinciding with the natural

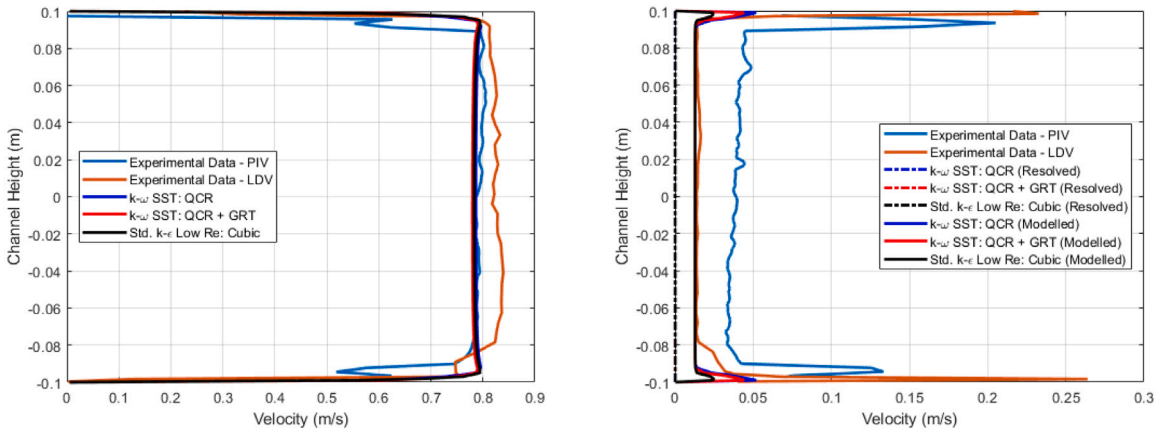

(a) Mean Velocity (b) RMS Velocity Fluctuation

Fig. 10. Mean and RMS fluctuation streamwise velocity profiles at a vertical section 140 mm ahead of cylinder1.

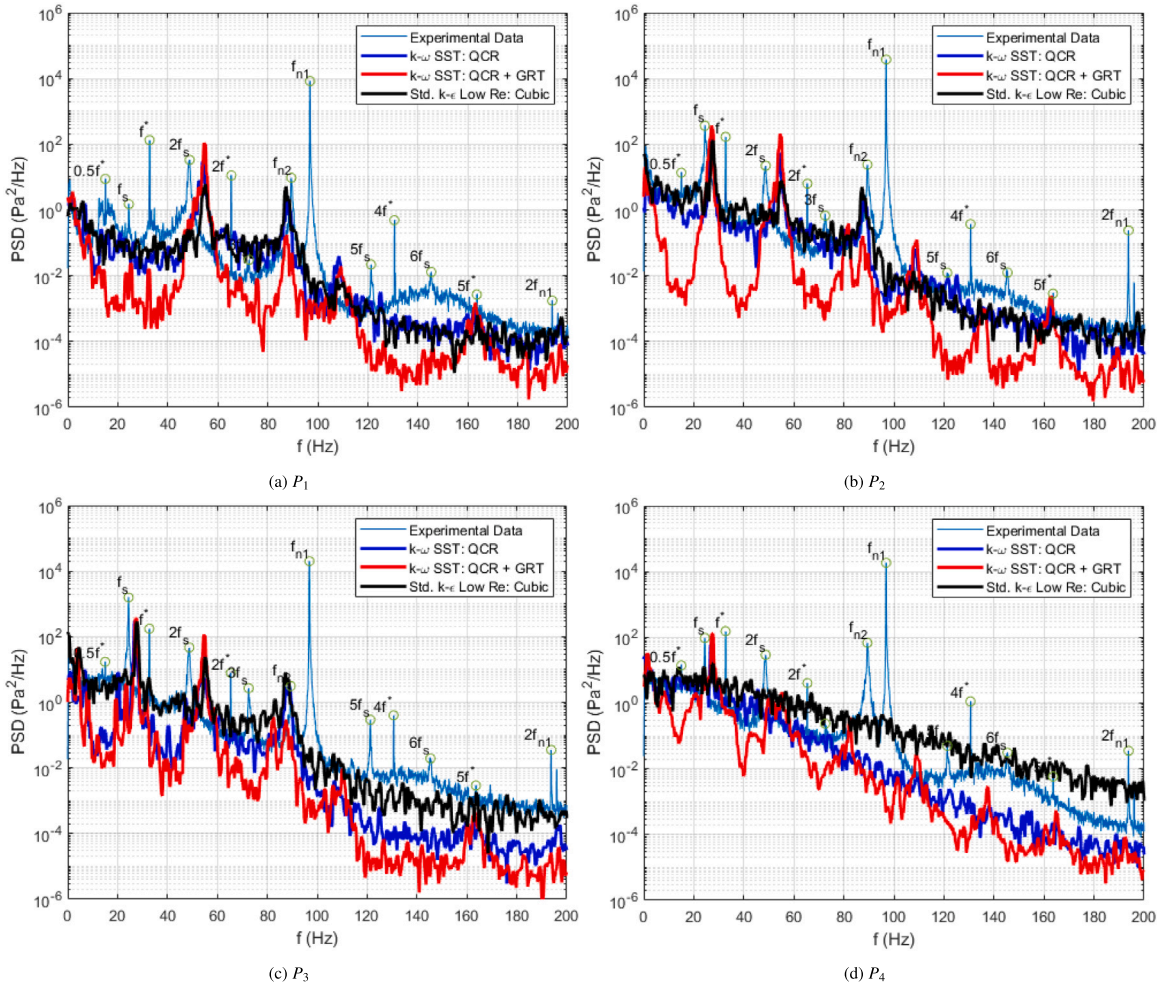

(a) P_1 (b) P_2

(c) P_3 (d) P_4

Fig. 11. Pressure spectra plots.

frequency of Cylinder1 (f_{n1}) and the fourth harmonic of f_s, thereby corrupting the estimate of the spectral density at this frequency. Although this accounts for part of the gap in expectations, the main reason is suspected to be the fact that there is a mismatch in the predicted fourth harmonic of f_s and the natural frequency of Cylinder1 which is needed for resonance. The values for f_s predicted by the turbulence models are 27.04 Hz, 27.43 Hz and 27.81 Hz, respectively in the order as they appear in the plots, which translate to significant errors of 10.81%, 12.42% and 13.98%, respectively.

The second reason is the fact that the problem at hand is that of vibrations that are partly Vortex-Induced and partly Turbulence-Induced. Even if resonance is not captured, the presence of physical turbulence upstream of Cylinder1 could have caused a peak similar in magnitude to that of Cylinder2 which faces turbulence generated by Cylinder1. The fact that this is absent in the numerical simulation has

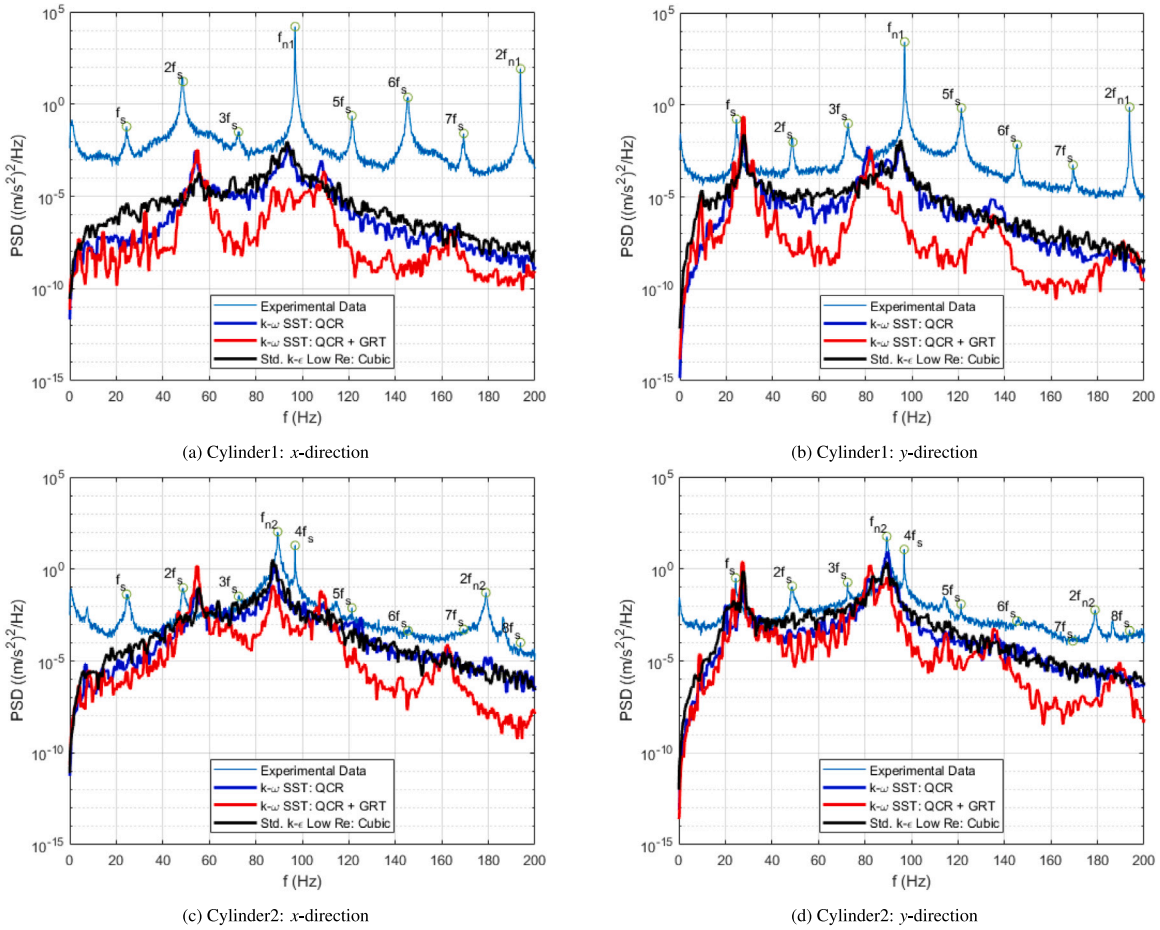

(a) Cylinder1: x-direction

(b) Cylinder1: y-direction

(c) Cylinder2: x-direction

(d) Cylinder2: y-direction

Fig. 12. Acceleration spectra plots for the cylinders.

likely led to a prediction of spectral density at f_{n1} at the level of the background spectra of frequencies.

Coming to the turbulence models, it is observed that the spectral densities at the peaks are similar for the two K-ω SST models. However, it is observed that the background spectra for the other frequencies are severely underpredicted for the QKWT model although it helps in identifying the peaks easily. As for the CKE model, the spectra obtained for P_1 and P_2 matches closely with the QKW model. For P_3 and P_4, however, the spectra predicted by the CKE model has a higher background spectra which makes it a better fit for P_3 in the higher frequency range while it leads to an overprediction for P_4. In fact for P_4, no expected peak is clearly distinct from the background spectra for this model. This implies that by the time the turbulence generated at the cylinders arrives at the location of P_4 which is 50 mm aft of Cylinder2, the vortical structures have broken down to structures of several time scales and thereby frequencies with similar contributions of spectral density appear in Fig. 11.

The acceleration spectra of the cylinders obtained from the experiment and numerical simulations are shown in Fig. 12. The experimental results for Cylinder1 and Cylinder2 reveal distinct peaks at f_s and its multiples as well as the natural frequencies f_{n1} and f_{n2} in both streamwise or drag (x) and cross flow or lift (y) directions. The numerical results show distinct peaks corresponding to the even harmonics of f_s in the x-direction and the odd harmonics of f_s in the y-direction. The numerical results also show peaks for f_{n1} and f_{n2} in both directions.

Overall, for the spectra of Cylinder1, the numerical results are severely underpredicted especially at f_{n1} which is expected to have a high value owing to resonance. As was reasoned earlier, the mismatch in peak spectral density of f_{n1} is suspected to be primarily due to the mismatch in the fourth harmonic of f_s and f_{n1} while the background spectra mismatch is owed to the absence of physical turbulence upstream of Cylinder1. For Cylinder2, the obtained results match well in terms of the spectral density at the peaks, especially f_{n2}, as well as the background spectra. This is owing to the off-resonant condition of Cylinder2 and the presence of turbulence generated by Cylinder1.

Coming to the individual turbulence models, the QKWT model agrees well with its QKW counterpart in terms of the peaks but underpredicts the background spectra as was earlier seen in the pressure spectra plots. This could be attributed to less breakdown of vortical structures and thereby a more 2D vortex shedding behaviour. This assertion will be addressed later when discussing the vorticity plots. The other two models provide similar spectra with the CKE model offering a slightly higher background spectra in comparison.

The predictions of f_s by the turbulence models are confirmed to be the same values quoted from the pressure spectra plots. The natural frequency of Cylinder1 is predicted to be 96 Hz from the y-direction spectra while it is predicted to be 95 Hz in the x-direction which translates to errors of 2.04% and 3.06%, respectively. Similarly, the natural frequency of Cylinder2 is predicted to be 90 Hz from the y-direction spectra while it is predicted to be 89 Hz in the x-direction which translates to errors of 0.12% and 1.14%, respectively. Further improvements can be made in the prediction of f_{n1} at the cost of f_{n2} by reducing the lengths of the bobs further. Another way would be to reduce the lengths of the bobs in Cylinder1 alone which would result in non-identical structures for the cylinders. These suggested modifications, however, are not made in the current study.

The time history plots of the cylinder tip displacements as measured on the same locations as the acceleration probes (see Fig. 6(b)) are presented in Fig. 13. No measurement was made in the experiment and thus it is not possible to validate the obtained displacements.

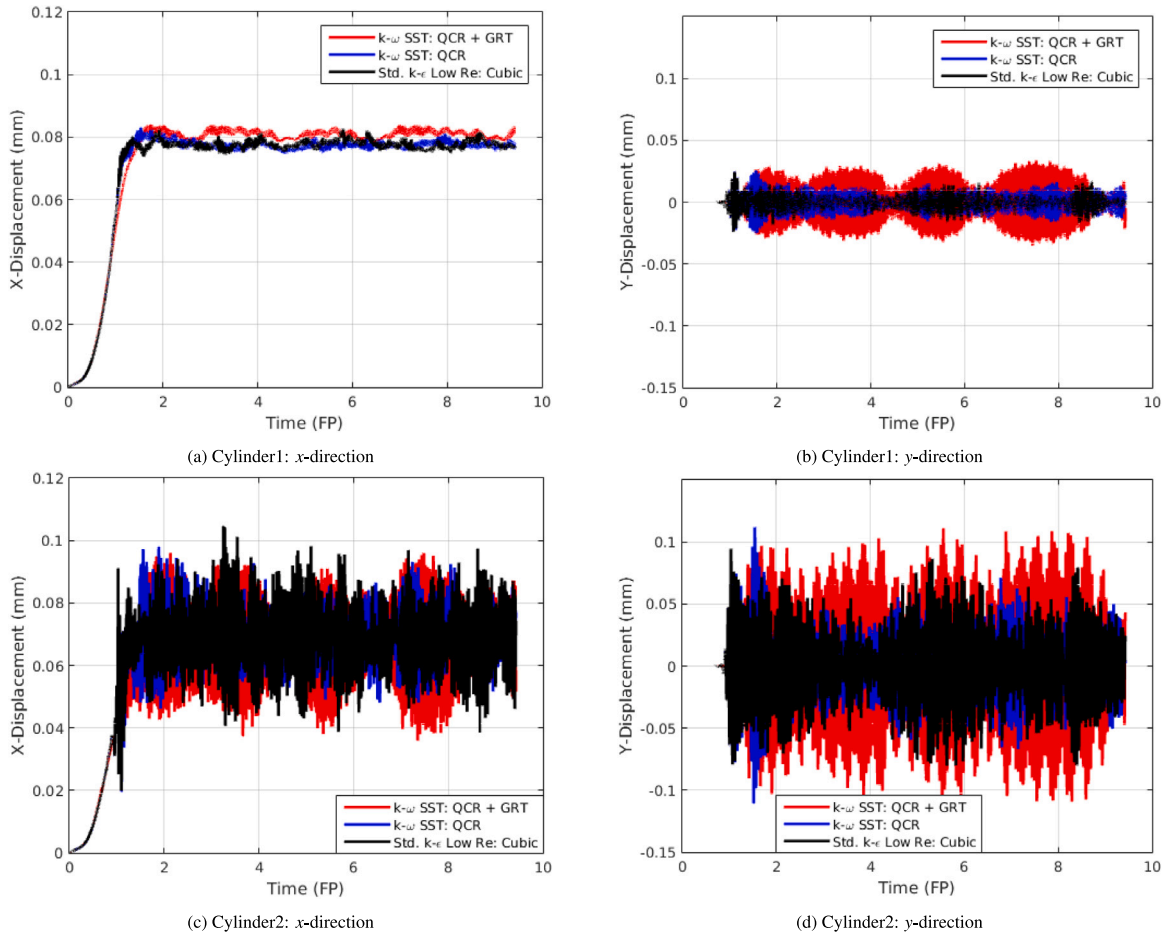

(a) Cylinder1: x-direction

(b) Cylinder1: y-direction

(c) Cylinder2: x-direction

(d) Cylinder2: y-direction

Fig. 13. Displacement plots for the cylinders.

Table 8
RMS vibration amplitudes.

Model	Cylinder1		Cylinder2	
	x-direction (μm)	y-direction (μm)	x-direction (μm)	y-direction (μm)
QKW	0.9299	7.1230	7.2159	21.8725
QKWT	1.2596	16.6918	11.8637	54.8572
CKE	1.2538	5.4085	10.0719	29.4507

The numerical results unanimously predict larger vibration amplitudes in both directions for Cylinder2 compared to Cylinder1, contrary to what one would expect given that this is the peak resonance case for Cylinder1. This is again reasoned to be owing to the absence of physical turbulence upstream of Cylinder1, the mismatch of the fourth harmonic of f_s and f_{n1} and the fact that Cylinder2 experiences the turbulence generated by Cylinder1. The RMS vibration amplitudes predicted by the models are presented in Table 8.

The velocity spectra plots for different turbulence models at a few select locations are shown along with the experimental results in Fig. 14. The spectra, in principle, captures the turbulence present in the flow from the inlet (relevant for all planes) as well as that generated at the channel walls (relevant for planes Z_1 and Z_3), the cylinder curved surface (relevant for all planes) and the 2 mm gap at the free end of the cylinder (relevant for plane Z_1). To obtain clean spectra plots, linear averaging is applied with a window size of 30, 5 and 3 for the LDV and PIV experimental results and numerical results, respectively. The experimental results show peaks for f_s and different harmonics. Not all peaks are distinct with some expected peaks being at the same level as the background spectra.

Similar trends are also seen for the numerical results with the spectra towards higher frequencies (> 100 Hz) showing underpredicted results especially for plane Z_1 (see Fig. 14(b)). This is expected since higher frequencies imply smaller time scales and thereby smaller turbulent structures which cannot be accurately resolved with the current choice of time step, meshes and the URANS scheme. For the current choice of parameters, however, the CKE model shows the best agreement in the high frequency range at all locations, especially at plane Z_1 which is a critical zone given the influence of the turbulence generated at the free end of the cylinder in the 2 mm gap between the channel wall.

Another observation is the mismatch in predictions of f_s in the experiment and the numerical results. The predictions for f_s at V_1^i and V_3^i were found to be the same as V_2^i and V_4^i, respectively. The experimental as well as numerical predictions for f_s are thus tabulated in Table 9 for V_1^i and V_3^i.

The numerical results are in close agreement with the experimental results. The largest difference between the predictions of the turbulence models are observed at plane Z_1 with the least error offered by the CKE model. The tabulated numerical results, although encouraging, go against the expectation of observing an overestimation of f_s as was observed in the pressure and acceleration plots. One possible reason is the error in picking the peak as caused by the applied linear averaging

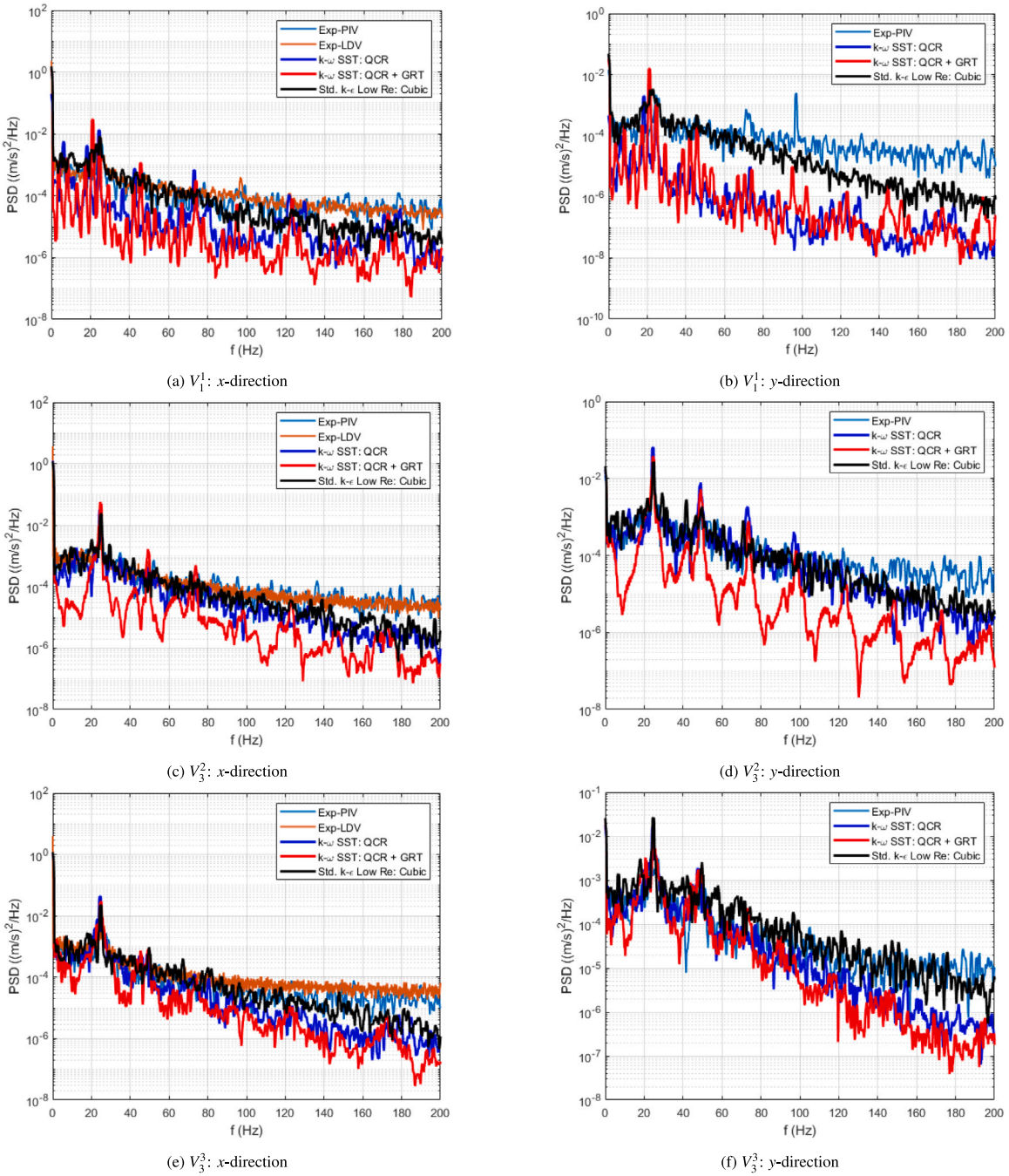

(a) V_1^1: x-direction

(b) V_1^1: y-direction

(c) V_3^2: x-direction

(d) V_3^2: y-direction

(e) V_3^3: x-direction

(f) V_3^3: y-direction

Fig. 14. Select velocity spectra plots: V_i^j, $(i, j = 1, 2, 3,$ as per Fig. 6(a)).

process to make a cleaner spectra plot. Using the averaging process does make the signal less noisy but it also flattens out the tips of the peaks. Thus, the "peaks" actually span as wide as 1.5 Hz for some curves inducing significant error in picking out the true frequency.

As was brought up earlier when discussing the spectra prediction for the high frequency range, it was asserted that the accuracy is linked to better resolving small scale turbulent structures. Thus the expectation is to have a well captured turbulent wake for the CKE model as well as the QKW model with perhaps a near 2D vortex shedding for the QKWT model. The expectation is checked against the vorticity plots created at the end of the simulation as shown in Figs. 15 and 16 (shorthand for turbulence models is same as Table 9).

As can be observed from Fig. 15, the expectation is confirmed with respect to the type of wake captured by the turbulence models. The CKE model and the QKW model predict vortex tubes being shed from Cylinder1 with these regular structures starting to break down into smaller ones as they travel towards Cylinder2. As they interact with Cylinder2 and its generated wake, visually, the regular structures appear nearly lost as per the QKW model and completely lost as per the

Table 9
Vortex shedding frequency predictions by the experiment and FSI test cases.

	f_s at V_1^1 (Hz)				f_s at V_1^2 (Hz)				f_s at V_1^3 (Hz)			
	Exp.	QKW	QKWT	CKE	Exp.	QKW	QKWT	CKE	Exp.	QKW	QKWT	CKE
x	25.1	24.5	24.5	24.7	24.3	24.4	24.4	24.5	25.1	23.8	23.8	25.0
y	24.7	24.3	24.7	24.7	24.3	24.4	24.4	24.5	25.1	23.8	23.8	25.0
	f_s at V_3^1 (Hz)				f_s at V_3^2 (Hz)				f_s at V_3^3 (Hz)			
	Exp.	QKW	QKWT	CKE	Exp.	QKW	QKWT	CKE	Exp.	QKW	QKWT	CKE
x	24.6	21.4	21.4	23.5	24.7	24.3	24.5	24.5	26.6	24.7	25.0	25.0
y	24.9	21.3	21.1	23.1	24.5	24.3	24.5	24.5	26.8	24.7	25.0	25.0

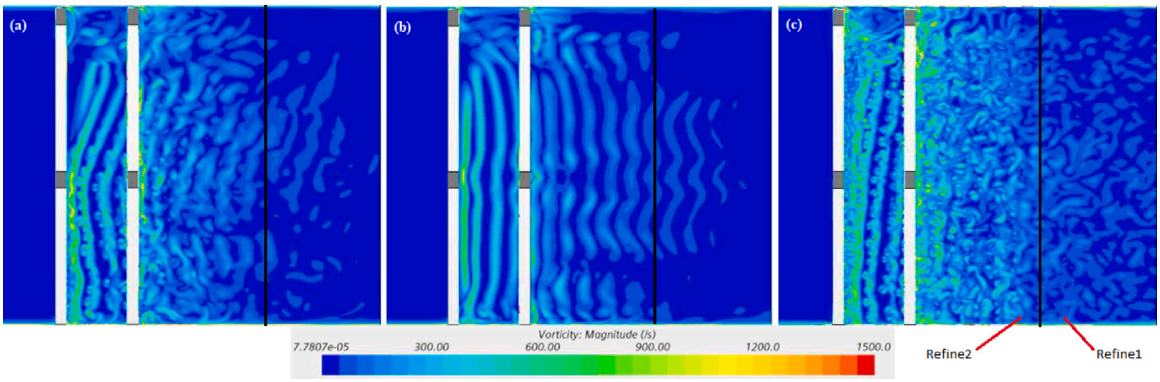

Fig. 15. Vertical section vorticity plots for (a) QKW (b) QKWT and (c) CKE.

CKE model. The QKWT model, on the other hand, predicts near regular structures even aft of Cylinder2.

It is also to be noted that part of the wake aft Cylinder2 appears to be subject to numerical dissipation as the vortical structures pass over from Refine2 to Refine1 refinement regions of the mesh about $10D$ aft of Cylinder2. This can be observed as a drop in the strength of vorticity as it passes over the interface of the refinement regions and is more clearly noticed in Fig. 15c. This is attributed to the vorticity being recomputed with new (and less accurate) approximations to the derivatives of the velocity for the coarse region. This adversely affects the results but is expected to be at a low degree given the location of this issue and is thus tolerated. Improvements in the results can be expected for having a longer Refine2 refinement region but is not carried out in the current study.

The last set of results are the mean and RMS fluctuation velocity profiles at horizontal sections 10 mm ($1.43D$) and 20 mm ($2.86D$) behind each of the cylinders, a select few of which are shown in Fig. 17. The mean velocity profiles are a consequence of the cylinders obstructing the flow at the centre of the channel width with the fluid squeezing through the remaining width of the channel at a higher-than-inlet velocity as per the continuity equation. For all planes, the velocity profile tends to flatten out as it gets away from the cylinders. This is owed to the internal viscous forces between fluid layers of different velocity as they try to reorient the profile back to the shape that existed ahead of the cylinders. Finally, differences are also noted in the profiles for different planes at a given location. This is owed to the fact that the problem is 3D with the cylinders having a finite length, the presence of channel walls and the 2 mm gap between the cylinder tips and the channel wall.

All simulation results also show good agreement with the experimental results at all locations and planes with the exception of the QKW profile 20 mm behind Cylinder1 at plane Z_1 (see Fig. 17(c)) and the CKE profile 10 mm behind Cylinder1 at plane Z_2 (not shown for brevity) as they predict a larger dip in mean velocity at the centre of the channel width.

Unlike for the mean velocity profile plots, the PIV and LDV experimental results are not as well in agreement with each other for the fluctuation plots. This is especially true for planes Z_2 and Z_3. The LDV results are selected for asserting the trends and for comparison against the simulation results.

The fluctuation profiles reveal significant resolved fluctuations near the centre of the channel width with the fluctuations gradually decreasing towards the channel walls and it slightly increasing again in the near vicinity of the channel walls. These fluctuations in velocity are owed to the vorticity in the flow. The centre of the channel width is subject to the turbulent wake of the cylinders while in the near vicinity of the wall, there exists the boundary layer which, in this case, is also interacting with the wake of the cylinders. In particular, there are two peaks observed at an offset from the centre of the channel width which is a consequence of the geometry of the vortex shedding process from the cylinder at this flow rate. The vortices shed from the top half and bottom half of the cylinders do not appear exactly in the centre but at an offset which can be observed from Fig. 16. The peak fluctuations near the centre of the channel width also appear to reduce with distance away from the cylinders. This is owed to the dissipation of vorticity and thereby a decrease in the strength of vorticity as it travels downstream from the cylinders. As the strength of the wake reduces, so do the fluctuations.

The numerical results capture the same number of peaks in the fluctuations as the experiment, however they clearly differ in their magnitudes compared to each other as well as the experiment. Unlike the mean profiles, the fluctuation profiles are visibly asymmetric for CKE which is not expected for this symmetric problem. Withstanding this slight asymmetry, the CKE model is observed to provide the best fit with the experimental results at all locations and planes.

Considering all qualitative and quantitative results, the CKE model is selected for the blind phase of the study on account of better modelling the wake of the cylinders which leads to more accurate spectra plots and velocity profile plots, especially the fluctuation profiles.

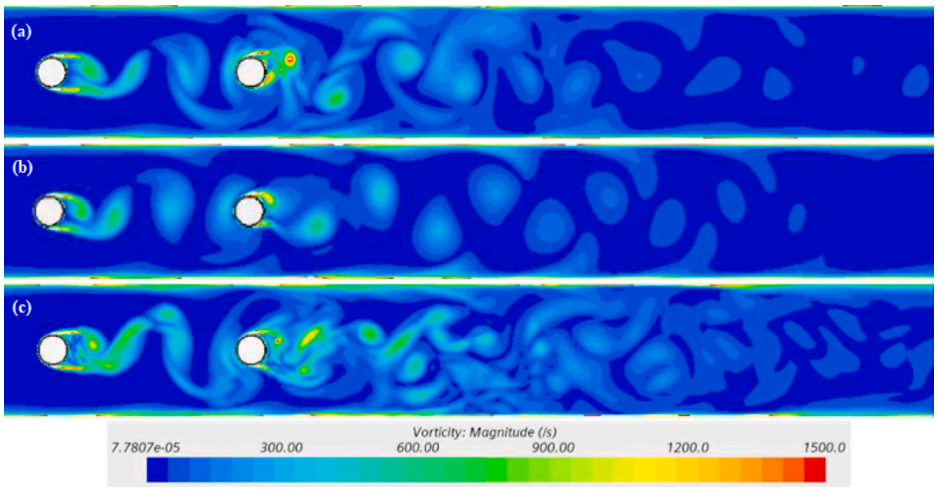

Fig. 16. Horizontal section vorticity plots for (a) QKW (b) QKWT and (c) CKE at Plane Z_2.

The current study has revealed certain shortcomings of the URANS scheme for predicting VIV, or as was reasoned in this case, a combination of VIV and TIV. While this scheme works well for off-resonant systems (in this case, Cylinder2), it does not work well to capture resonance particularly for FSI problems that have resonance of the structural natural frequency with higher harmonics of the vortex shedding frequency (in this case, Cylinder1). This is owing to the error of the URANS scheme in predicting the vortex shedding frequency which gets amplified for higher harmonics leading to a mismatch in predicting resonance. As a consequence, one would only capture resonance in the current study at a lower flow rate where the corresponding 'over-predicted vortex shedding frequency' would be lower. Even so, that would only solve half the problem as the TIV part of the spectra would still require actual turbulent fluctuations in velocity and pressure to be present from the inlet and that is something that the current scheme cannot provide as is. It is thus the expectation that these shortcomings will also be reflected in the results of the blind phase that is presented in the following section.

5. Blind phase

With the best suited turbulence model (Standard K-ϵ Low Re: Cubic) selected, the blind phase of the OECD/NEA benchmark is now discussed. The current study is mainly used to confirm the expectation mentioned at the end of the previous section. Given that in this phase, both off-resonant and resonant inflow rates will be tested, this is also a platform to further test the URANS framework and discuss the difference in responses for the two inflow rates.

The experimental setup and parameters of interest are given in Section 3. As with the open phase, the structural model is fine tuned via the brass mounting lengths and is discussed as part of the numerical setup in Section 5.1. Once the setup parameters and the meshes are selected, the finalized turbulence model is put the test against the FSI problem in Section 5.2.

5.1. Numerical setup

Based on the CAD drawings for the test section (and its contents) of the experimental setup, the simulation domain is set up in STAR-CCM+. The problem is set up with identical fluid, solid and FSI solver settings as the open phase. With the exception of the inlet boundary condition, the other boundary conditions for fluid and solid are also the same as the open phase. For the inlet, a time-varying uniform velocity is prescribed for the numerical stability of the current FSI study as given by:

$$u(0,y,z,t) = \begin{cases} u(0,y,z)\frac{1-\cos\left(\frac{\pi}{T}t\right)}{2}, & \text{if } t < T \\ u(0,y,z), & \text{otherwise} \end{cases}$$

$$u(0,y,z) = \begin{cases} 0.74 \text{ m/s}, & \text{Off-Resonance} \\ 1.62 \text{ m/s}, & \text{Resonance} \end{cases} \tag{29}$$

$$T = \begin{cases} 0.75\,\text{s}\,(1.01\,FP), & \text{Off-Resonance} \\ 0.7\,\text{s}\,(2.06\,FP), & \text{Resonance} \end{cases}$$

The fluid mesh is created using the same approach as in the open phase. The target base size of the mesh is 3 mm and is reduced by half as one crosses over each refinement region sequentially. Care is taken to ensure a y^+ value of 1 on all walls as per the resonant inflow velocity. The same mesh is thus used for the off-resonant case as well. The mesh so created has 7.78M elements whose sectional views are shown below in Fig. 18(a).

The solid mesh is created using the same approach as in the open phase. The mesh for the cylinders are quad dominant with 3 elements along the thickness having a total cell count of about 276k for each cylinder. The bobs are filled with a quad dominant mesh with 40 and 80 layers having a total cell count of 21k and 44k for those housed in Cylinder1 and Cylinder2, respectively. Sectional views of the solid mesh are shown in Fig. 18(b). For low computational effort, linear finite elements are employed.

Before proceeding to the FSI simulations, there is a need to fine tune the structures to the experimental vibrational frequencies. For the experimental study, it was mentioned that the brass bobs were 14 mm and 29 mm in length excluding the solder. As with the open phase, the structural model is fine tuned by altering the length of the bobs. Numerically testing the vibrations of select cylinder model candidates in vacuum and water, the final choice is made to proceed with a bob length pair of 15 mm and 30 mm. The results for different choices of bob length are shown in Tables 10 and 11. To address the mismatch in damping ratio, which is more significant for Cylinder2, the aforementioned 'Rayleigh Damping' model is employed as described in the open phase. With this, all relevant parameters for the FSI study are finalized and the results obtained for the same are discussed in the following subsection.

5.2. FSI study

With the selected mesh and the fine tuned structural model, the FSI test is attempted for the off-resonance case of 0.74 m/s inflow and

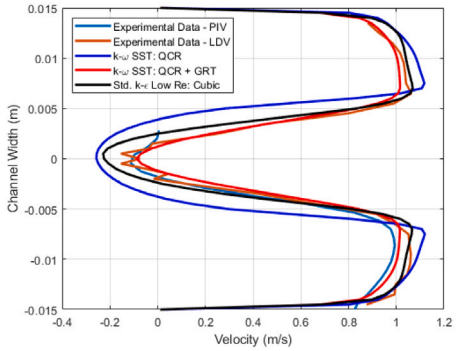

(a) Plane Z_1: Mean Velocity 10 *mm* behind Cylinder1

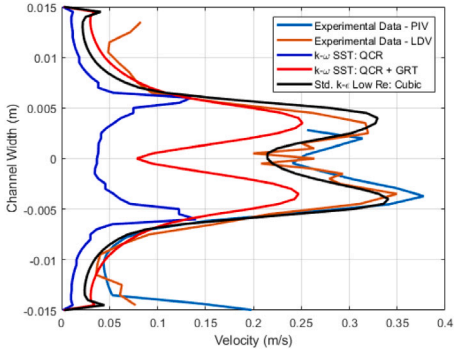

(b) Plane Z_1: RMS Velocity Fluctuation 10 *mm* behind Cylinder1

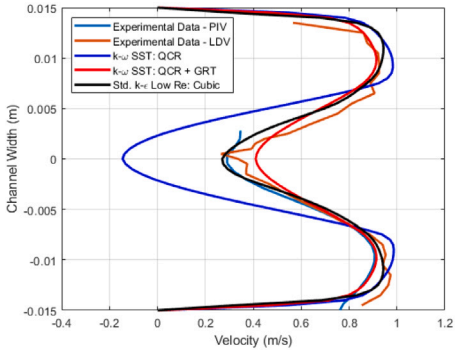

(c) Plane Z_1: Mean Velocity 20 *mm* behind Cylinder1

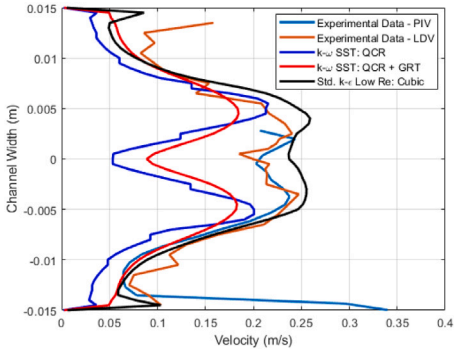

(d) Plane Z_1: RMS Velocity Fluctuation 20 *mm* behind Cylinder1

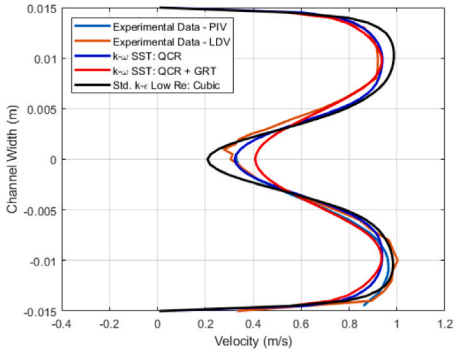

(e) Plane Z_2: Mean Velocity 10 *mm* behind Cylinder2

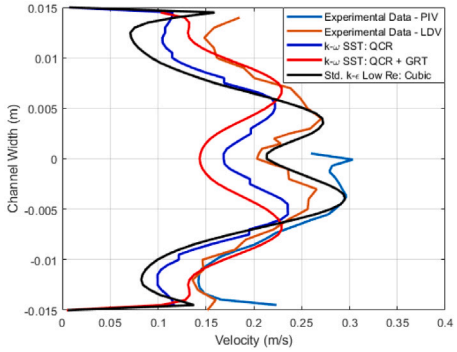

(f) Plane Z_2: RMS Velocity Fluctuation 10 *mm* behind Cylinder2

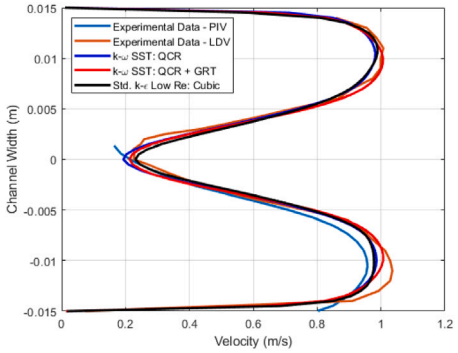

(g) Plane Z_3: Mean Velocity 10 *mm* behind Cylinder2

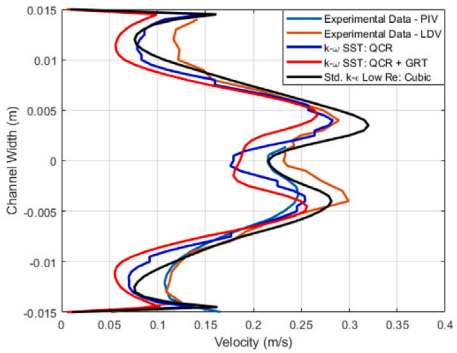

(h) Plane Z_3: RMS Velocity Fluctuation 10 *mm* behind Cylinder2

Fig. 17. Mean and RMS fluctuation streamwise velocity profiles at horizontal sections in plane Z_i $(i = 1, 2, 3)$.

the peak resonance case of 1.62 m/s inflow using the shortlisted CKE turbulence model. To keep the FSI coupling stable during the start up of the simulation, a cosine ramping of the inflow velocity is given as per Eq. (29). A total simulation time of 11.3855 s (15.334 FP) is provided for the off-resonance case while 5.5 s (16.204 FP) is provided for the peak resonance case.

Since the experimental vortex shedding frequency is unknown for the blind phase, Strouhal estimates of the same are made as per $f_s = St \cdot U/D$. Based on the pitch to diameter ratio $P/D = 4.5$, the expected Strouhal Numbers for both cylinders are expected to be lower than that of a single isolated cylinder [40,41]. As a conservative estimate, a value of $St = 0.21$ is adopted conforming to that of a single isolated cylinder. The expected vortex shedding frequencies are thus 15.6 Hz and 34.0 Hz

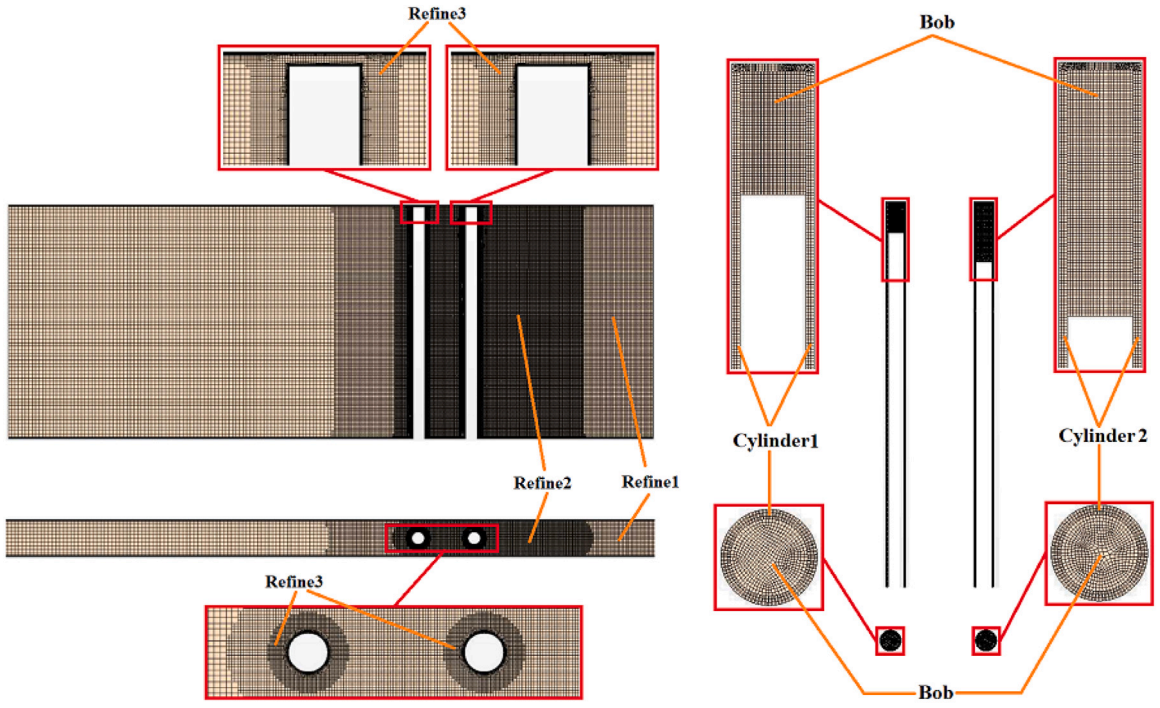

(a) Fluid Mesh (b) Solid Mesh

Fig. 18. Sectional views of the fluid and solid mesh.

Table 10
Results for vibration tests in vacuum.

Pairs of boblengths (mm)	Natural frequency (Hz)	
	Cylinder1	Cylinder2
14.0, 29.0	186.34	169.97
15.0, 30.0	185.19	168.77
Exp. Soln.	183.90	168.80

Table 11
Results for vibration tests in water.

Pairs of bob lengths (mm)	Natural frequency (Hz)		Damping ratio	
	Cylinder1	Cylinder2	Cylinder1	Cylinder2
14.0, 29.0	166.67	155.04	0.0023	0.0012
15.0, 30.0	165.29	154.44	0.0031	0.0012
Exp. Soln.	164.90	153.00	0.0035	0.0035

for the off-resonance case and peak-resonance case, respectively. To adhere to the 100 sampling point thumb rule, a time step size of 0.75 ms is used during the cosine ramping and is reduced to 0.5 ms for the remainder of the simulation for the off-resonance case while corresponding values of 0.35 ms and 0.24 ms are used for the peak resonance case. Using the back-windowing approach on the created spectra plots, it was found that transient results lasted 2 FP after the end of the cosine ramping period. Thus results corresponding to the last 14 FP for both cases are used for creating the spectra. Based on a similar analysis to the open phase, an inflow turbulence level of 10% is selected.

5.2.1. Obtained results

The primary results of interest for the FSI study are the velocity, acceleration and pressure spectra for the points as per Fig. 6. The pressure spectra plots for the off-resonance ('OR') case and the peak resonance ('R') case are shown along with the experimental results in Fig. 19. To obtain clean spectra plots, linear averaging is applied with a window size of 30 for the experimental results, 15 and 10 for the OR and R cases, respectively. The experimental results show several peaks that correspond to multiples of the vortex shedding frequency (f_s = 21.81 Hz [OR], 39.89 Hz [R]) and the natural frequency of Cylinder1 (f_{n1} = 160.4 Hz) and Cylinder2 (f_{n2} = 152.4 Hz). The other distinct peaks in the experimental results are suspected to be linked with the pump frequency.

As the flow rate is increased, the PSD levels increase for both the experimental and numerical results. However, the numerical results show overpredicted background spectra levels by an order of magnitude. This was also observed to a lesser extent for the prediction of P_4 in the open phase FSI test (see Fig. 11(d)). The reasoning given in the open phase about the cause being the redistribution of peak spectral densities to higher frequencies with the breakdown of turbulence to smaller scales does not seem as plausible here.

For the natural frequency of the cylinders, only that of Cylinder2 is distinct as was the case in the open phase FSI study. The absence of actual turbulence from the inlet in the simulation for both flow rates is suspected to be the reason why Cylinder1 is not excited for the off-resonance case. For the peak resonance case, this reason along with the fact that the vortex shedding frequency is overpredicted, is suspected to have caused an even larger gap between the experimental and numerical results. The vortex shedding frequencies predicted here are 22.93 Hz and 48.76 Hz which translate to relative errors of 5.13% and 22.24% for the off-resonance and peak resonance cases, respectively.

Not all harmonics of f_s are distinct for the numerical solution. For P_1, only the first even harmonic is distinct while for P_2 and P_3, only the first harmonic is distinct for the peak resonance case while the first three harmonics are distinct for the off-resonance case. For P_4, no harmonic of f_s is captured for either of the two cases. These observations are in line with those for the open phase FSI study where it was reasoned to imply an easier propagation of the frequency pertinent to the streamwise direction (even harmonics) than it is for the cross flow (odd harmonics) and that the first harmonic is more easily captured immediately downstream of the source (the cylinders) rather than upstream.

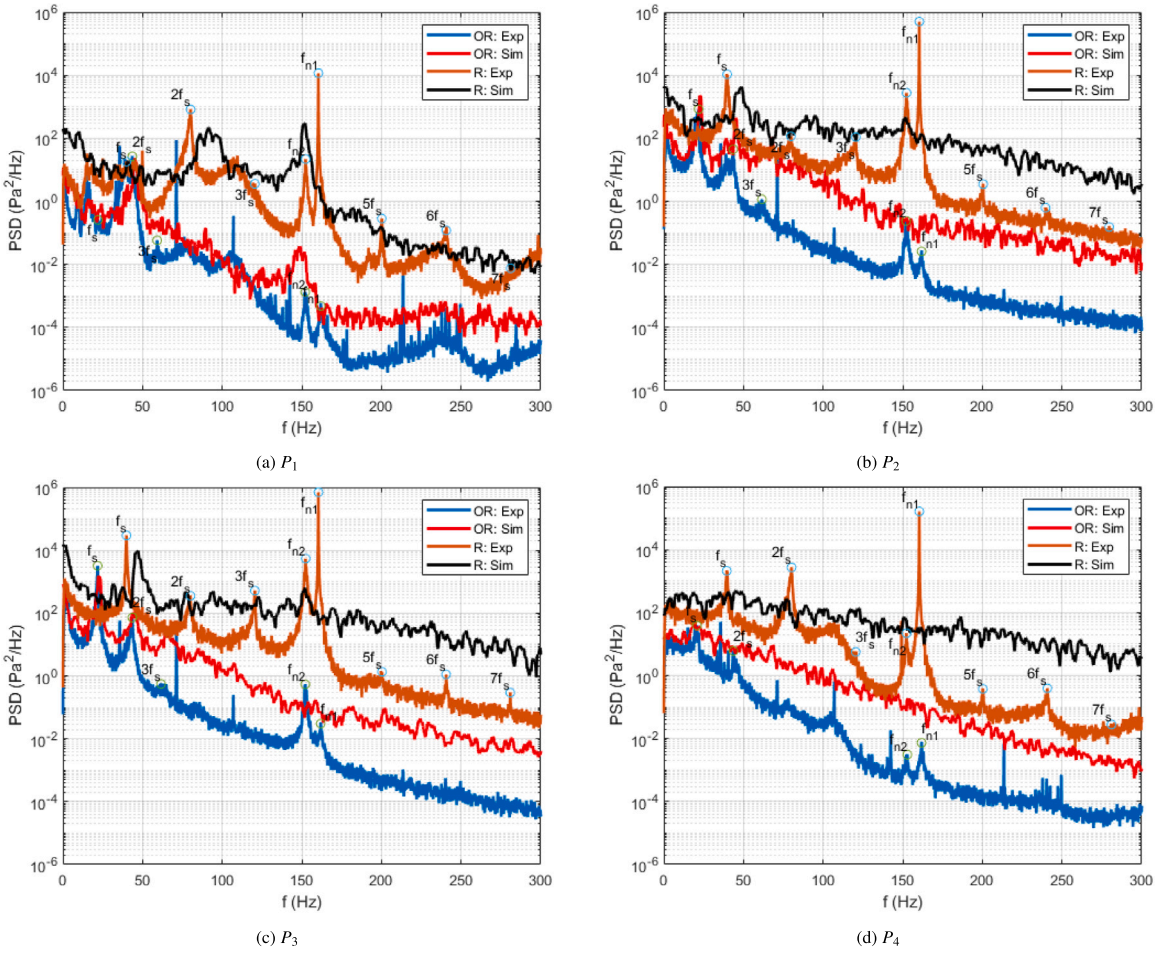

(a) P_1 (b) P_2

(c) P_3 (d) P_4

Fig. 19. Pressure spectra plots.

The acceleration spectra of the cylinders obtained from the experiment and numerical simulations are shown in Fig. 20. The same linear averaging is applied here as the pressure spectra plots. The experimental results for Cylinder1 and Cylinder2 reveal distinct peaks at f_s and its multiples as well as f_{n1} and f_{n2} in both streamwise (x) and cross flow (y) directions. The numerical results show distinct peaks corresponding to the even harmonics of f_s in the x-direction and the odd harmonics of f_s in the y-direction. The numerical results also show peaks for f_{n1} and f_{n2} in both directions.

For the spectra of Cylinder1, the numerical results are underpredicted for both the off-resonance and peak resonance conditions. At f_{n1}, the error is of 2 orders of magnitude in the x-direction and of 3 orders of magnitude in the y-direction for the off-resonance case. The error is more severe for the peak resonance case with corresponding errors of 5 orders of magnitude in the x-direction and 4 orders of magnitude in the y-direction. For the peak resonance case, the mismatch of the fourth harmonic of f_s with f_{n1} is suspected to be the main reason as was stated while reasoning the open phase FSI results. Even so, the other reason was reasoned to be the absence of inlet turbulence that could explain the gap in the results of the off-resonance case and that of the background spectra of the peak resonance case.

For Cylinder2, the match in the background spectra is much better for both the cases with underpredictions in the higher frequency range. The match is much better for Cylinder2 owing to the presence of actual turbulence generated from Cylinder1. As was reasoned for the open phase FSI study, having better predictions in the high frequency range requires a smaller time step, grid size and even a higher fidelity method such as LES instead of URANS. Even though the background spectra overlaps with the experimental curve in the low frequency range, the peak spectral density at f_{n2} is still underpredicted. At f_{n2}, the error is of 1 order of magnitude in the x-direction while it is of 2 orders of magnitude in the y-direction for the off-resonance case. The error is about the same for the peak resonance case with corresponding errors of 1 order of magnitude in the x- and y-direction. The error is comparatively less compared to Cylinder1 on account of the fact that Cylinder2 is always in an off-resonance condition for both cases.

The predictions of the numerical f_s are confirmed to be the same values quoted from the pressure spectra plots. The natural frequency of Cylinder1 is predicted to be 164.6 Hz from the y-direction spectra while it is predicted to be 160.5 Hz in the x-direction which translates to errors of 2.61% and 6.23E−2%, respectively. Similarly, the natural frequency of Cylinder2 is predicted to be 151.4 Hz from the y-direction spectra while it is predicted to be 152.1 Hz in the x-direction which translates to errors of 0.66% and 0.20%, respectively. The fine tuned structural model is thus confirmed to give the correct value for the natural frequency of the cylinders. Improving the prediction of the same warrants further modification of the pairs of bob lengths which is not carried out in this study.

The time history plots of the cylinder tip displacements are presented in Fig. 21. No measurement was made in the experiment and thus it is not possible to validate the obtained displacements. The observations of the current results match those observed for the open phase. The RMS vibration amplitudes predicted by the models are presented in Table 12. There is a clear increase of RMS vibration as the flow rate is increased as expected.

A selection of velocity spectra plots for the two cases are shown along with the experimental results (available only in the x-direction) in Fig. 22. The same linear averaging is applied here as the pressure

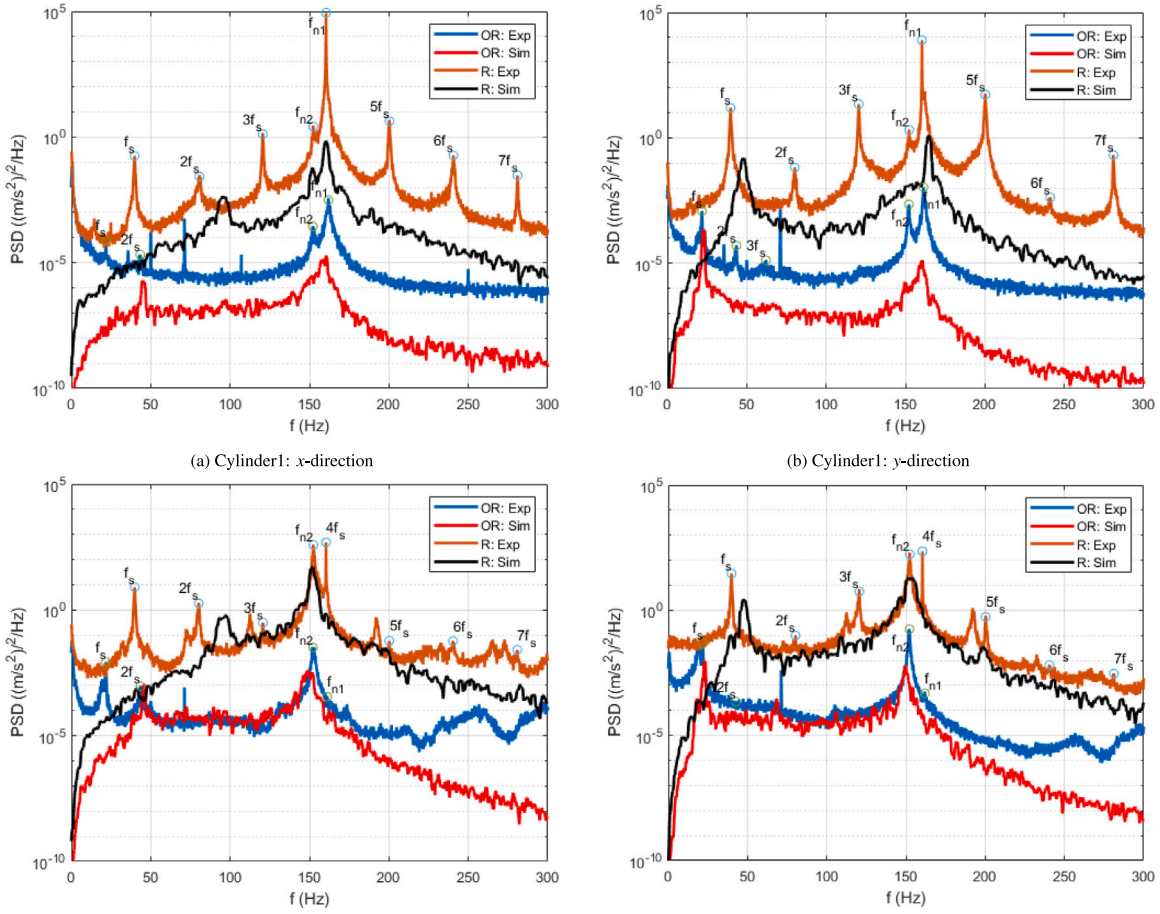

(a) Cylinder1: x-direction

(b) Cylinder1: y-direction

(c) Cylinder2: x-direction

(d) Cylinder2: y-direction

Fig. 20. Acceleration spectra plots for the cylinders.

Table 12
RMS vibration amplitudes.

Case	Cylinder1		Cylinder2	
	x-direction (μm)	y-direction (μm)	x-direction (μm)	y-direction (μm)
OR	0.2587	1.0187	0.9887	6.6582
R	2.6353	9.3752	22.5858	40.4036

and acceleration spectra plots. The experimental results show peaks for f_s and its harmonics. Not all peaks are distinct, however, with some expected peaks being at the same level as the background spectra. Similar trends are observed for the numerical results with the spectra towards higher frequencies showing underpredicted results.

The underprediction of the background spectra begins earlier for the off-resonance case (at 105 Hz on average) than it does for the peak resonance case (at 220 Hz on average). However, looking at these numbers as multiples of f_s for each case reveals that the match in the background spectra is till about the fifth harmonic of f_s. As reasoned earlier for the acceleration spectra as well as the corresponding plots for the open phase FSI study, a higher fidelity method along with smaller mesh size and time step is warranted for seeing improvements in the prediction as the small scale turbulence gets resolved better.

The vortex shedding frequency is again overpredicted for both the off-resonance and peak resonance cases. Comparing the spectral density at f_s shows predictions of the same order of magnitude as the experimental results at all planes for the off-resonance case and plane Z_3 for the peak resonance case while there is an order of magnitude difference for planes Z_1 and Z_2 for the peak resonance case. It is also observed that the f_s captured by the experiment as well as the numerical results vary slightly along the length of the cylinders. In particular, the predictions at V_1^i and V_3^i were found to be the same as V_2^i and V_4^i, respectively. The experimental as well as numerical predictions for f_s are tabulated in Table 13 for V_1^i and V_3^i with corresponding (x-direction) relative errors tabulated in Table 14.

The experimental results show similar values for f_s at all locations for the peak resonance case. For the off-resonance case, the results are similar for planes Z_1 and Z_2 while there is a drop in the value at plane Z_3. The numerical results, on the other hand, predict a higher value at plane Z_2 compared to planes Z_1 and Z_3 at all locations. From Table 14, the largest errors are observed to be at plane Z_3 for the off-resonance case and at plane Z_2 for peak resonance case. In general, the errors are found to be higher for the peak resonance case than the off-resonance case.

Although experimental results are not available for the y-direction, the simulation results are tabulated in Table 13. The prediction of f_s is observed to be the same as that obtained from the x-direction velocity spectra for all locations except V_3^1 for both cases and at V_3^2 for the peak resonance case where the y-direction prediction is higher than that of the x-direction. It is to be noted that all the values quoted from the simulation have an uncertainty of about ±1.5 Hz in selecting the f_s owing to the flattening of the peak tips by the linear averaging process as was mentioned in the open phase FSI study. Withstanding this, the expectation from the open phase study of overpredicting f_s for the peak resonance case is considered to be met.

A final observation from the velocity spectra trends is that the peaks were more distinct 10 mm behind the cylinders (V_1^i and V_3^i) rather than 20 mm behind the cylinders (V_2^i and V_4^i, not shown here in the interest of brevity) with peaks being more distinct for V_1^i as compared

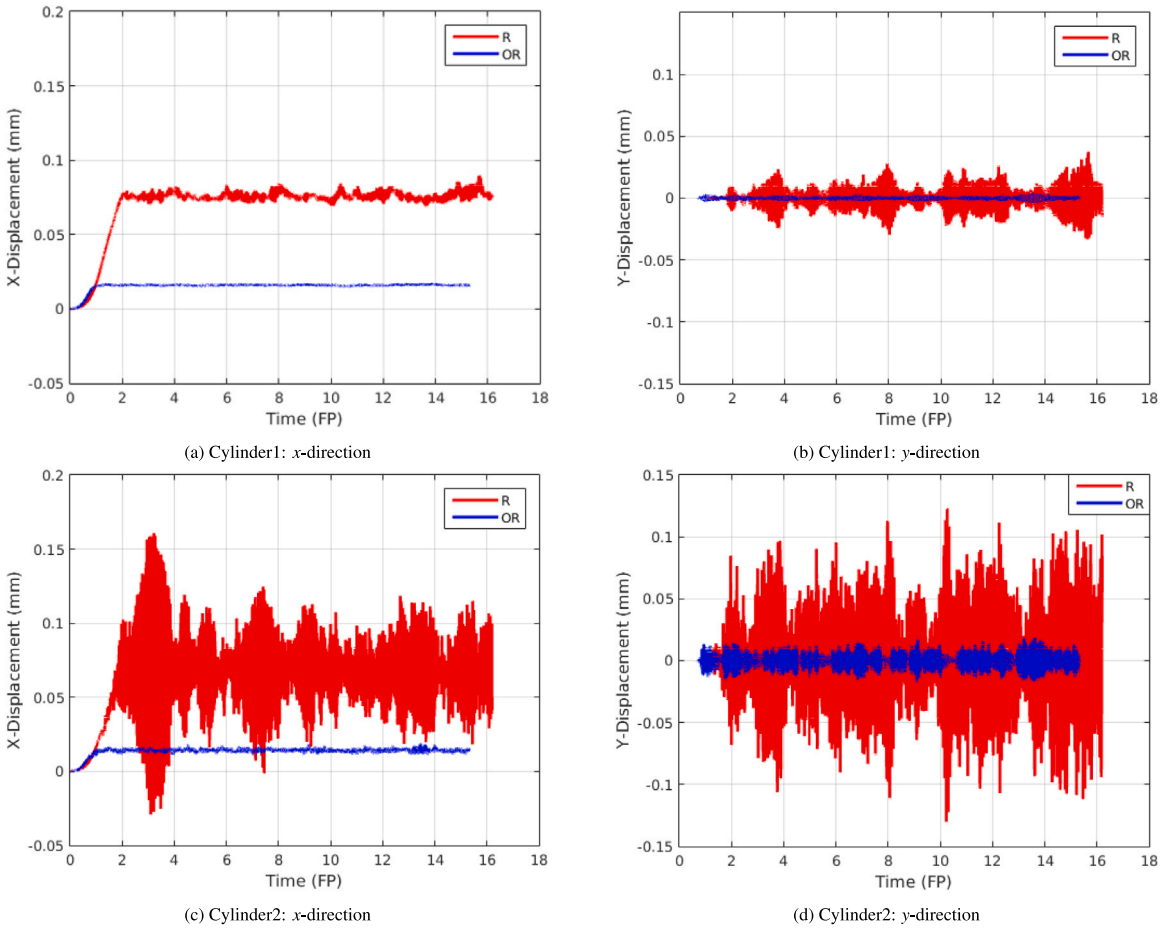

(a) Cylinder1: x-direction

(b) Cylinder1: y-direction

(c) Cylinder2: x-direction

(d) Cylinder2: y-direction

Fig. 21. Displacement plots for the cylinders.

Table 13
Vortex shedding frequency predictions by the experiment and the simulation.

OR	f_s at V_1^1 (Hz)		f_s at V_1^2 (Hz)		f_s at V_1^3 (Hz)		f_s at V_3^1 (Hz)		f_s at V_3^2 (Hz)		f_s at V_3^3 (Hz)	
	Exp.	Sim.	Exp.	Sim.	Exp.	Sim.	Exp.	Sim.	Exp.	Sim.	Exp.	Sim.
x	21.5	21.2	21.5	22.6	19.0	22.1	21.3	20.6	21.6	22.8	19.7	22.3
y	–	21.7	–	22.6	–	22.0	–	21.4	–	22.7	–	22.2
R	f_s at V_1^1 (Hz)		f_s at V_1^2 (Hz)		f_s at V_1^3 (Hz)		f_s at V_3^1 (Hz)		f_s at V_3^2 (Hz)		f_s at V_3^3 (Hz)	
	Exp.	Sim.	Exp.	Sim.	Exp.	Sim.	Exp.	Sim.	Exp.	Sim.	Exp.	Sim.
x	39.9	46.4	40.0	47.1	40.7	44.7	40.1	42.7	40.0	44.4	40.0	44.2
y	–	46.4	–	47.1	–	44.7	–	45.1	–	47.3	–	44.4

Table 14
Relative errors in predicting the vortex shedding frequency by the simulation.

Test case	V_1^1 (%)	V_1^2 (%)	V_1^3 (%)	V_3^1 (%)	V_3^2 (%)	V_3^3 (%)
OR	1.395	5.116	16.316	3.286	5.556	13.197
R	16.291	17.750	9.828	6.484	11.000	10.500

to V_3^i. As was reasoned in the open phase FSI study, this is linked to the dissipation of vortical structures as they travel downstream and the presence of a source of turbulence (Cylinder1) upstream of Cylinder2. This is hinted by the vorticity plots shown in Figs. 23 and 24.

As was also observed from the open phase FSI study, vortex tubes are shed from Cylinder1 with these regular structures breaking down into smaller ones as they travel towards Cylinder2. As they interact with Cylinder2 and its generated wake, the regular structures visually appear to be completely lost for both the off-resonance and peak resonance cases. The turbulent structures are observed to have higher strength for the peak resonance case than the off-resonance case. This is expected since vorticity ($\vec{\omega} = \nabla \times \vec{U}$) scales with direction-derivatives of velocity which increase with increasing flow rate aft of the cylinders.

To confirm the similarity of the wake of the two cases, the vorticity is non-dimensionalized by f_s which incorporates the influence of the flow rate via the Strouhal number. The non-dimensional vorticity plots so created are shown in Figs. 25 and 26. The near similar non-dimensional strength of the wake thus confirms the similarity of the wake for the off-resonance and peak resonance cases.

The last set of results are the mean and RMS fluctuation velocity profiles at horizontal sections 10 mm ($1D$) and 20 mm ($2D$) behind each of the cylinders, a select few of which (only plane Z_2) are shown in Fig. 27. The explanation for the shape of these plots has already been discussed for the open phase FSI study. The PIV and LDV curves for the mean and RMS fluctuation velocity profiles are observed to agree with each other at all planes and locations of measurement.

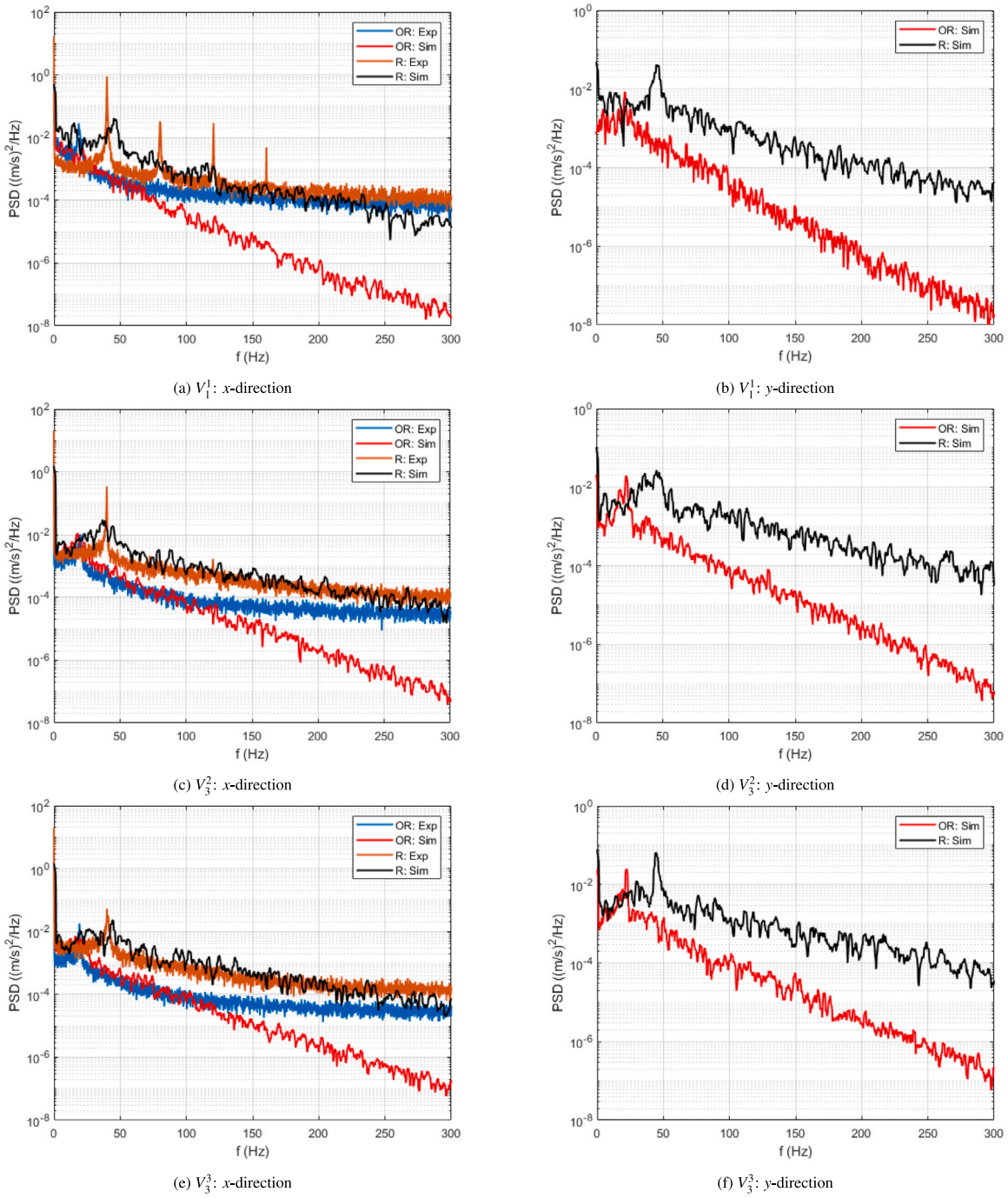

(a) V_1^1: x-direction

(b) V_1^1: y-direction

(c) V_3^2: x-direction

(d) V_3^2: y-direction

(e) V_3^3: x-direction

(f) V_3^3: y-direction

Fig. 22. Velocity spectra plots: V_i^j, $(i, j = 1, 2, 3,$ as per Fig. 6(a)).

The mean velocity profiles predicted for the off-resonance case qualitatively appears to match the experimental results well with the largest deviation observed for the profile 10 mm behind Cylinder1 at plane Z_2 (see Fig. 27(a)) as a larger dip in mean velocity at the centre of the channel width is predicted. On the other hand, the profiles for the peak resonance case have more deviations from the experimental profiles. In general, it is observed that the agreement between the numerical prediction and experimental results improves as the distance from the source of turbulence (cylinders) is increased. This observation holds for both the off-resonance and peak resonance cases.

The observations for the RMS fluctuation profiles are observed to be similar to those of the mean profiles with a better match for the off-resonance case predictions than the peak resonance case predictions with the corresponding experimental curves. The other observation of improving results with increasing distance from the cylinders seems to hold for the off-resonance case but not so for all solutions of the peak resonance case (see Figs. 27(b) and 27(d) for example).

The current study attests to the shortcomings of the URANS scheme for predicting VIV, or as was reasoned earlier, a combination of VIV and TIV. The current scheme showed underpredicted spectra results for

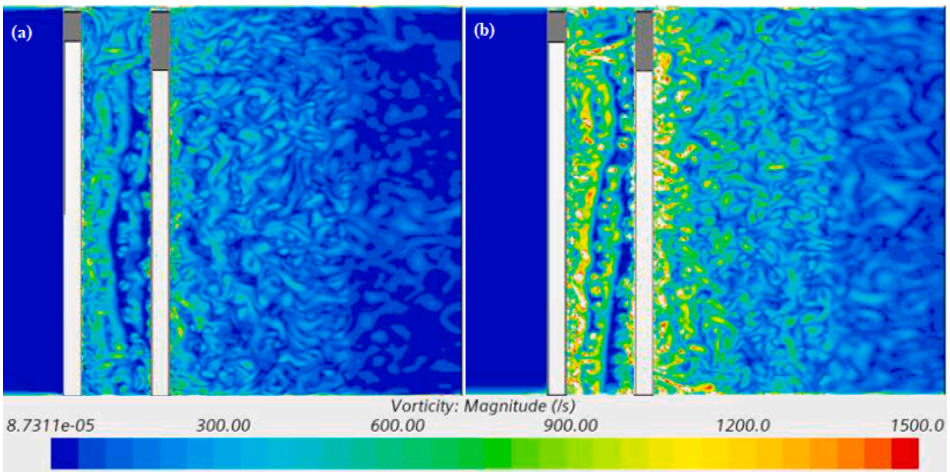

Fig. 23. Vertical section vorticity plots for (a) OR and (b) R test cases.

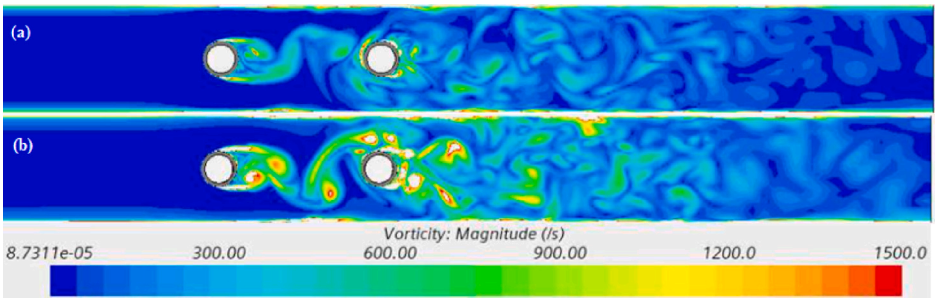

Fig. 24. Horizontal section vorticity plots for (a) OR and (b) R test cases at plane Z_2.

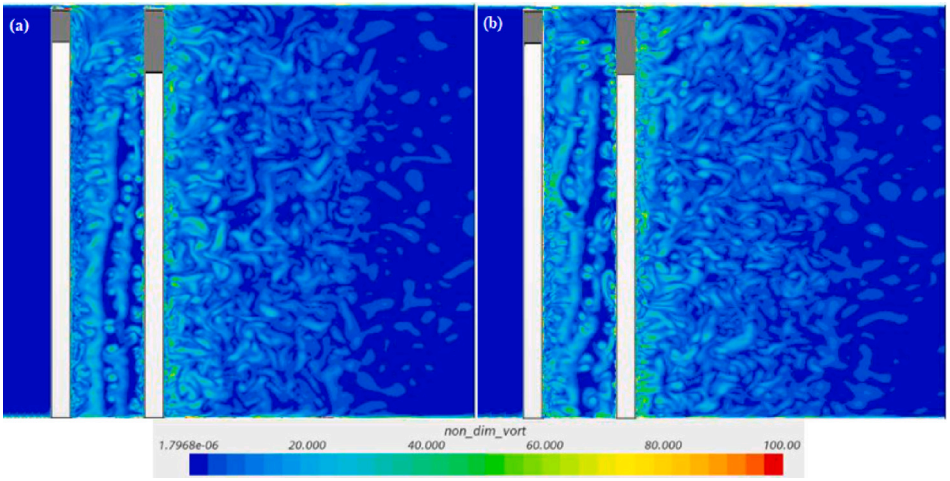

Fig. 25. Vertical section non-dimensional vorticity plots for (a) OR and (b) R test cases.

Cylinder1 in both the off-resonance and peak resonance cases. This was accompanied with an overprediction of the vortex shedding frequency. The results were better for Cylinder2 spectra plots, although the peak at its natural frequency was still underpredicted as was the spectral density for the higher frequency range.

With the observations of the current study corroborating those of the open phase study, the following gaps for the URANS scheme in predicting a combination of VIV and TIV still stand:

- Prediction of the vortex shedding frequency: For systems that suffer from the lock-in effect between the structural natural frequency and higher harmonics of the vortex shedding frequency, accurate prediction of the vortex shedding frequency appears to be an important criteria.
- Inflow turbulence: For systems that suffer from significant TIV contributions, it appears important to incorporate actual or modelled fluctuations of velocity and pressure (in essence turbulence) to capture accurate background spectra levels.
- Predicting high frequency range spectra: To capture the high frequency range correctly, it is requisite to capture the small scale turbulence in the flow.

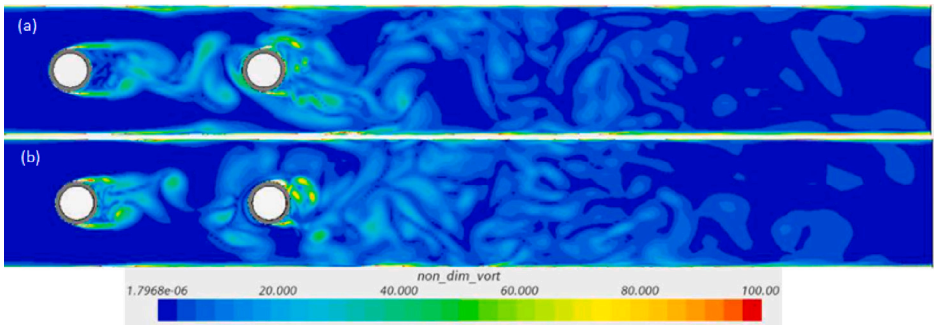

Fig. 26. Horizontal section non-dimensional vorticity plots for (a) OR and (b) R test cases at plane Z_2.

The above gaps still serve as a hypothesis for the cause of the difference between the experimental and numerical FSI results for the open and blind phase. Additional tests are to be conducted to confirm this hypothesis. These future tests are recommended along with key conclusions from the current work in the following section.

6. Conclusions

This work was set to tackle the Vortex-Induced Vibration (VIV) problem of in-line cantilevered cylinders subjected to cross flow as was proposed in the form of a benchmark by the WGAMA of the OECD/NEA. To carry out this FSI study, the computationally cheaper URANS framework was selected over DNS or LES in order to test its efficacy in the prediction of VIV by selecting the best suited URANS model (and associated settings) and establishing the gap between this model and the available experimental data. The OECD/NEA benchmark came in 2 phases: the open phase where experimental results were available from the beginning and the blind phase where the experimental results were only released after all participants handed in their results.

The open phase of the study was used to select the most appropriate turbulence model for the blind phase. Key observations for the open phase were (1) The overprediction of the vortex shedding frequency, (2) Severely underpredicted spectral density at the natural frequency of Cylinder1 where resonance is expected as well as low background spectra levels, (3) Better fit for the Cylinder2 spectra and (4) Underprediction for all spectra plots in the higher frequency range. Based on these observations, it was hypothesized that a major cause for the difference in numerical and experimental predictions of Cylinder1 is a combined effect of the mismatch in the fourth harmonic of vortex shedding frequency and its natural frequency as well as the absence of actual turbulence (in terms of velocity and pressure fluctuations) from the inlet. To improve upon the prediction of the higher frequency range of the spectra, a higher fidelity method accompanied with a smaller grid and time step size is suggested. From the results obtained in this phase of the study, the Standard K-ϵ Low Re: Cubic model is finalized.

The blind phase results were similar in behaviour to the open phase study. Additionally, the off-resonance results corroborated the aforementioned cause with underpredicted results for Cylinder1 and better fitting results for Cylinder2. From this study, gaps were identified in the capability of URANS in capturing VIV or as was reasoned for the OECD/NEA benchmark, a combination of TIV and VIV where the lock-in effect is dependent on a higher harmonic of the vortex shedding frequency. These are in short:

1. Predicting the vortex shedding frequency accurately.
2. Providing actual inflow turbulence.
3. Predicting high frequency range spectra accurately.

6.1. Recommendations for future work

With the current gaps identified, the pathway for future work can be set in different directions. These are provided below:

1. Using the finite strain approximation for solid displacement: It is expected to have an effect on the wake produced at the free end of the cylinders which would in turn influence the displacement.
2. Confirming and quantifying the lock-in effect artificially: This could be done by either increasing the natural frequency (by virtue of the bob length, for instance) or decreasing the flow velocity. The gap between the spectral density at the new peak and the experimental results will help quantify the effect of missing out on lock-in.
3. Confirming and quantifying the TIV contribution: The Pressure Fluctuation Model (PFM) that was proposed in the works of Kottapalli [42] and Sharma [43] and further improved by van den Bos [44] could be modified to flood in fluctuations for the cross flow OECD/NEA benchmark problem within the scope of the URANS framework.
4. Higher fidelity approaches: These could be LES or hybrid models such as DES. Another recently developed hybrid model is the Scale Resolving Hybrid (SRH) model given by Duffal et al. [45] which is also available in STAR-CCM+ from V2020 onwards.

CRediT authorship contribution statement

M.M.M.D. Hussain: Writing – review & editing, Writing – original draft, Visualization, Methodology, Investigation, Formal analysis, Data curation, Conceptualization. **K. Zwijsen:** Writing – review & editing, Supervision, Resources, Project administration, Funding acquisition. **A.H. van Zuijlen:** Writing – review & editing, Visualization, Supervision, Methodology.

Declaration of competing interest

The authors declare the following financial interests/personal relationships which may be considered as potential competing interests: M.M.M.D. Hussain reports financial support was provided by Dutch Ministry of Economic Affairs and Climate. If there are other authors, they declare that they have no known competing financial interests or personal relationships that could have appeared to influence the work reported in this paper.

Acknowledgements

The authors gratefully acknowledge the PIONEER research program funded by the Dutch Ministry of Economic Affairs and Climate and thank the OECD/NEA for administering the benchmark.

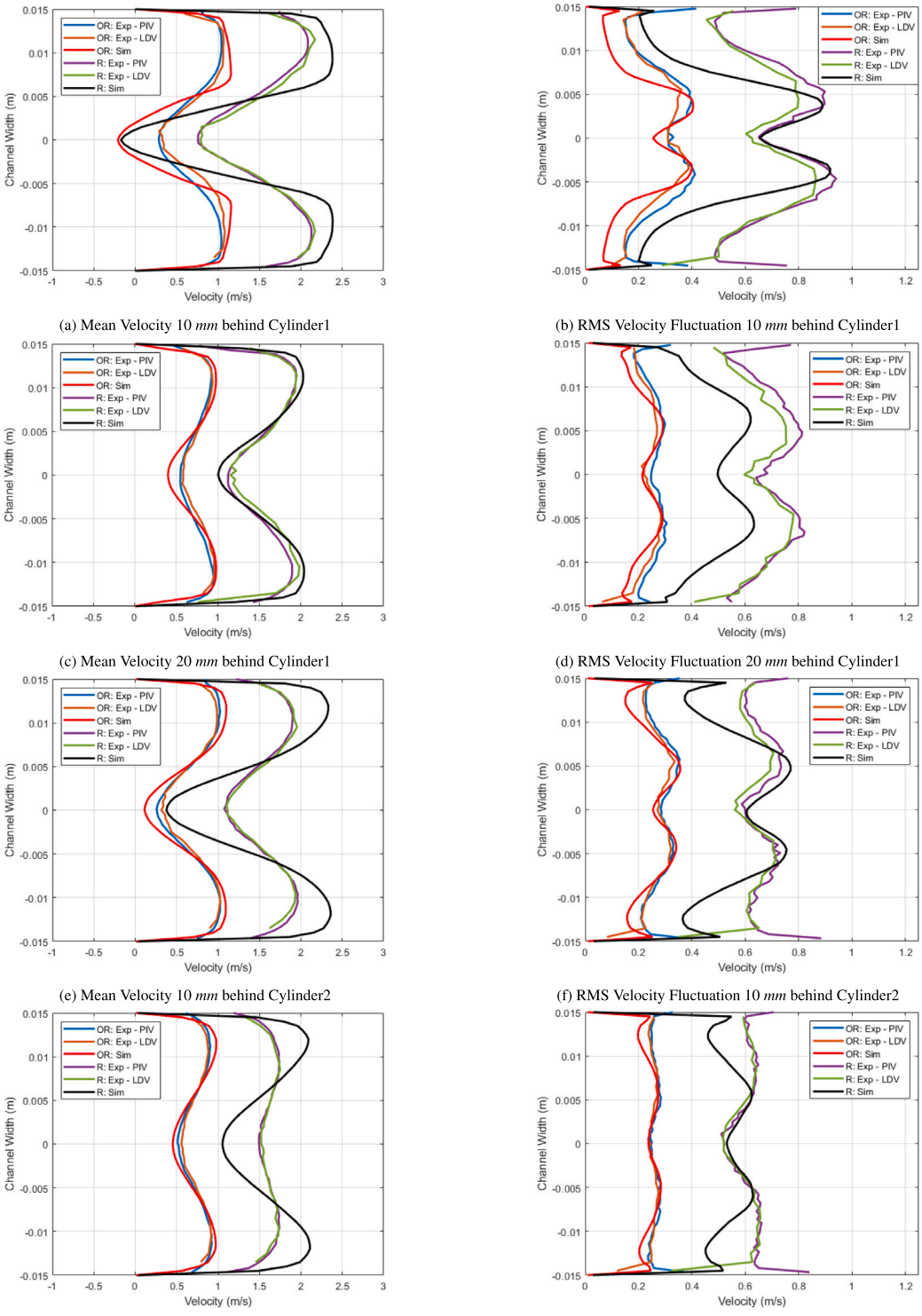

(a) Mean Velocity 10 *mm* behind Cylinder1

(b) RMS Velocity Fluctuation 10 *mm* behind Cylinder1

(c) Mean Velocity 20 *mm* behind Cylinder1

(d) RMS Velocity Fluctuation 20 *mm* behind Cylinder1

(e) Mean Velocity 10 *mm* behind Cylinder2

(f) RMS Velocity Fluctuation 10 *mm* behind Cylinder2

(g) Mean Velocity 20 *mm* behind Cylinder2

(h) RMS Velocity Fluctuation 20 *mm* behind Cylinder2

Fig. 27. Mean and RMS fluctuation streamwise velocity profiles at horizontal sections in plane Z_2.

Data availability

Data will be made available on request.

References

[1] IPCC. Global warming of 1.5 °C. Switzerland: IPCC; 2018.
[2] BP. BP energy outlook 2019. 2019.
[3] IAEA. Energy, electricity and nuclear power estimates for the period up to 2050. 2018, IAEA Reference Data Series No. 1/38, Vienna, Austria.
[4] IEA. World energy outlook 2018. Paris, France; 2018.
[5] MIT. The future of nuclear energy in a carbon-constrained world. Boston, USA: MIT; 2018.
[6] OECD. The costs of decarbonisation: System costs with high shares of nuclear and renewables. 2019, OECD-NEA No. 7299, Paris, France.
[7] WNI. World nuclear industry status report. Paris, London: Mycle Schneider Consulting; 2018.
[8] Podest M. Plant performance: Reducing downtime. IAEA Bull 1984;26(3).

[9] Païdoussis MP. Real-life experiences with flow-induced vibration. J Fluids Struct 2006;22(6–7):741–55. http://dx.doi.org/10.1016/j.jfluidstructs.2006.04.002.

[10] Tijsseling AS. Fluid–structure interaction in liquid-filled pipe systems: sources, solutions and unsolved problems. IWDE report 02-05, Technische Universiteit Eindhoven; 2002.

[11] Luk KH. Pressurized-water reactor internals aging degradation study. Technical report, Oak Ridge National Laboratory; 1993.

[12] Kim KT. A study on the grid-to-rod fret-ting wear-induced fuel failure observed in the 16x16KOFA fuel. Nucl Eng Des 2010;240(4):756–62. http://dx.doi.org/10.1016/j.nucengdes.2009.12.014.

[13] Yoo Y, Kim K, Eom K, Lee S. Finite element analysis of the mechanical behavior of a nuclear fuel assembly spacer grid. Nucl Eng Des 2019;352:110179. http://dx.doi.org/10.1016/j.nucengdes.2019.110179.

[14] Weaver DS, Ziada S, Au-Yang MK, Chen SS, Païdoussis MP, Pettigrew MJ. Flow-induced vibrations in power and process plant components—Progress and prospects. J Press Vessel Technol 2000;122(3):339. http://dx.doi.org/10.1115/1.556190.

[15] Pettigrew MJ, Taylor CE, Fisher NJ, Yetisir M, Smith BAW. Flow-induced vibration: recent findings and open questions. Nucl Eng Des 1998;185(2–3):249–76. http://dx.doi.org/10.1016/s0029-5493(98)00238-6.

[16] Kaneko S, Nakamura T, Inada F, Kato M, Mureithi NW. Flow-induced vibrations. Classifications and lessons from practical experiences. Academic Press; 2014.

[17] Dobrucali E, Kinaci OK. URANS-based prediction of vortex induced vibrations of circular cylinders. J Appl Fluid Mech 2017;10(3):957–70. http://dx.doi.org/10.18869/acadpub.jafm.73.240.27339.

[18] Martini S, Morgut M, Pigazzini R. Numerical VIV analysis of a single elastically-mounted cylinder: Comparison between 2D and 3D URANS simulations. J Fluids Struct 2021;104:103303. http://dx.doi.org/10.1016/j.jfluidstructs.2021.103303.

[19] Ding L, Bernitsas MM, Kim ES. 2-D URANS vs. experiments of flow induced motions of two circular cylinders in tandem with passive turbulence control for 30 000<Re<105, 000. S. Ocean Eng 2013;72:429–40. http://dx.doi.org/10.1016/j.oceaneng.2013.06.005.

[20] Ding L, Zhang L, Kim ES, Bernitsas MM. URANS vs. experiments of flow induced motions of multiple circular cylinders with passive turbulence control. J Fluids Struct 2015;54:612–28. http://dx.doi.org/10.1016/j.jfluidstructs.2015.01.003.

[21] Wang P, Zhao W, Jiang J, Wang X, Li S, Luo X. Experimental and numerical investigations of flow-induced vibration of tube arrays subjected to cross flow. Int J Press Vessels Pip 2019;176:103956. http://dx.doi.org/10.1016/j.ijpvp.2019.103956.

[22] Vivaldi D, Baccou J. Flow-induced vibration simulations of a straight tube bundle in water cross-flow, through URANS approach. In: Proceedings of the pressure vessels & piping conference, volume 3: fluid-structure interaction; high pressure technology, Las Vegas, Nevada, U.S.A. July 17–22. ASME; 2022, http://dx.doi.org/10.1115/PVP2022-81757, V003T04A003.

[23] Benhamadouche S, Benguigui W. Wall-resolved LES and low-Reynolds number URANS combined to an arbitrary Lagrangian Eulerian approach for predicting water cross-flow induced vibrations of a single flexible tube in a normal square tube array. In: Proceedings of the 20th international topical meeting on nuclear reactor thermal hydraulics (NURETH-20), Washington D. C., U. S. A., August 20–25. 2023.

[24] OECD/NEA. Best practice guidelines for the use of CFD in nuclear reactor safety applications - revision. OECD/NEA Report NEA/CSNI/R(2014)11, 2014.

[25] OECD/NEA. The FSI benchmark based on OKBM experiments to validate coupled CFD and CSD calculations - NEA benchmark exercise. NEA/CSNI/R(2023)2, Paris: OECD Publishing; 2024.

[26] Bolshukhin MA, Budnikov AV, Shmelev EI, Kulikov DA, Loginov AV, Pribaturin NA, et al. Dynamic measurements of the flow and structure oscillations to validate FSI calculations. Nucl Eng Des 2021;381:111336. http://dx.doi.org/10.1016/j.nucengdes.2021.111336.

[27] Hussain MMMD, Zwijsen K, van Zuijlen AH, Roelofs F. URANS simulations for fluid-structure interaction of cylinders in cross-flow. In: Proceedings of the 19th international topical meeting on nuclear reactor thermal hydraulics. 2022.

[28] Vivaldi D. An assessment of CFD-scale fluid–structure interaction simulations through comprehensive experimental data in cross-flow. Comput Fluids 2024;278:106303. http://dx.doi.org/10.1016/j.compfluid.2024.106303.

[29] Pan Z, Cui W, Miao Q. Numerical simulation of vortex-induced vibration of a circular cylinder at low mass-damping using RANS code. J Fluids Struct 2007;23(1):23–37. http://dx.doi.org/10.1016/j.jfluidstructs.2006.07.007.

[30] Khan NB, Ibrahim Z, Khan MI, Hayat T, Javed MF. VIV study of an elastically mounted cylinder having low mass-damping ratio using RANS model. Int J Heat Mass Transfer 2018;121:309–14. http://dx.doi.org/10.1016/j.ijheatmasstransfer.2017.12.109.

[31] Esmaeili M, Rabiee AH. Active feedback VIV control of sprung circular cylinder using TDE-iPID control strategy at moderate Reynolds numbers. Int J Mech Sci 2021;(1065):202–315. http://dx.doi.org/10.1016/j.ijmecsci.2021.106515.

[32] Siemens. Simcenter STAR-CCM+ documentation. 2020, Version 2020.3. Available at https://docs.sw.siemens.com/en-US/product/226870983/doc/PL20200805113346338.starccmp_userguide_pdf/pdf/.

[33] Lien FS, Chen WL, Leschziner MA. Low-Reynolds-number eddy-viscosity modelling based on non-linear stress-strain/vorticity relations. Eng Turbul Model Exp 1996;91–100. http://dx.doi.org/10.1016/b978-0-444-82463-9.50015-0.

[34] Yap C. Turbulent heat and momentum transfer in recirculating and impinging flows [Ph.D. Dissertation], U.K.: Faculty of Technology, University of Manchester; 1987.

[35] Durbin PA. On the k-3 stagnation point anomaly. Int J Heat Fluid Flow 1996;17(1):89–90. http://dx.doi.org/10.1016/0142-727x(95)00073-y.

[36] Langtry RB. A correlation-based transition model using local variables for unstructured parallelized CFD codes [Ph.D. Dissertation], Germany: University of Stuttgart; 2006, http://dx.doi.org/10.18419/opus-1705.

[37] Menter FR, Langtry RB, Likki SR, Suzen YB, Huang PG, Völker S. A correlation-based transition model using local variables—Part I: Model formulation. J Turbomach 2006;128(3):413. http://dx.doi.org/10.1115/1.2184352.

[38] Bilosova A. Modal testing. Ostrava: Investment in Education Development; 2011.

[39] Zwijsen K, Roelofs F, Hussain MMMD, van Zuijlen AH. Numerical simulation of cantilever cylinders in cross-flow: Participation to the OECD/NEA fluid-structure interaction benchmark. In: Proceedings of the 12th international conference on flow-induced vibration. Paris-Saclay, France; 2022, July 5-8.

[40] Zdravkovich MM. REVIEW—Review of flow interference between two circular cylinders in various arrangements. J Fluids Eng 1977;99(4):618. http://dx.doi.org/10.1115/1.3448871.

[41] Xu G, Zhou Y. Strouhal numbers in the wake of two inline cylinders. Exp Fluids 2004;37:248–56. http://dx.doi.org/10.1007/s00348-004-0808-0.

[42] Kottapalli S. Numerical prediction of flow induced vibrations in nuclear reactors through pressure fluctuation modeling [Master thesis], The Netherlands: Delft University of Technology; 2016.

[43] Sharma S. Numerical study of turbulence induced vibrations using synthetic fluctuation field modeling in nuclear reactor applications [Master thesis], The Netherlands: Delft University of Technology; 2018.

[44] van den Bos N. Turbulence-induced vibrations prediction: through use of an anisotropic pressure fluctuation model [Master thesis], The Netherlands: Delft University of Technology; 2022.

[45] Duffal V, de Laage de Meux B, Manceau R. Development and validation of a hybrid RANS-LES approach based on temporal filtering. In: Proceedings of the ASME-jSME-KSME 2019 8th joint fluids engineering conference. Volume 2: computational fluid dynamics. San Francisco, California, USA; 2019, July 28-August 1, 2019.